

---

# DETECTING MICRO FRACTURES WITH X-RAY COMPUTED TOMOGRAPHY

---

A PREPRINT

Dongwon Lee,\* Nikolaos Karadimitriou, Matthias Ruf and Holger Steeb

Institute of Applied Mechanics (CE), University of Stuttgart, Pfaffenwaldring 7, D-70 569, Germany

## ABSTRACT

Studying porous rock materials with X-Ray Computed Tomography (XRCT) has been established as a standard procedure for the non-destructive visualization of flow and transport in opaque porous media. Despite the recent advances in the field of XRCT, some challenges still remain due to the inherent noise and imaging artefacts in the produced data. These issues become even more profound when the objective is the identification of fractures, and/or fracture networks. The challenge is the limited contrast between the regions of interest and the neighboring areas. This limited contrast can mostly be attributed to the minute aperture of the fractures. In order to overcome this challenge, it has been a common approach to apply digital image processing, such as filtering, to enhance the signal-to-noise ratio. Additionally, segmentation methods based on threshold-/morphology schemes can be employed to obtain enhanced information from the features of interest. However, this workflow needs a skillful operator to fine-tune its input parameters, and the required computation time significantly increases due to the complexity of the available methods, and the large volume of the data-set. In this study, based on a data-set produced by the successful visualization of a fracture network in Carrara marble with  $\mu$ -XRCT, we present the segmentation results from a number of segmentation methods. Three conventional and two machine-learning-based methods are evaluated. The segmentation results from all five methods are compared to each other in terms of segmentation quality and time efficiency. Due to memory limitations, and in order to accomplish a fair comparison, all the methods are employed in a 2D scheme. The output of the 2D U-net model, which is one of the adopted machine-learning-based segmentation methods, shows the best performance regarding the quality of segmentation and the required processing time.

**Keywords** Rock fracture,  $\mu$ -XRCT, image segmentation, machine learning, local threshold, Sato filtering, active contouring, random forest, U-net

## 1 Introduction

The adequate characterization and knowledge of the geometrical properties of fractures have a strong constructive impact on various engineering disciplines. In the field of reservoir management, due to the fact that fractures strongly influence the permeability and porosity of a reservoir, their properties, like network connectivity and mean aperture, play a decisive role [1, 2, 3], in the production and conservation processes of resources, such as methane [4] and shale oil [5]. Additionally, the geometry of the fracture network is an equally important property that needs to address in our efforts to properly characterize the stresses developing between tectonic plates [6] which, eventually, have a strong effect on the permeability of a reservoir [7, 8]. As one of the most straight-forward and effective ways of investigating such fracture properties, 3D visualization and consequent efficient extraction of various fracture, or fracture network, spatial properties, like length, aperture, tortuosity etc., has been increasingly employed.

X-Ray Computed Tomography (XRCT) has been adopted as a non-destructive method to observe such spatial properties, and it has become a standard procedure in laboratory studies [9, 10, 11, 12, 13]. Micro-X-Ray Computed Tomography ( $\mu$ -XRCT) offers the ability to visualize features on the micro-scale, without destroying the sample, since it is a

---

\*Corresponding author: dongwon.lee@mechbau.uni-stuttgart.de

non-invasive visualization method. However, as with every other visualization method, there are some drawbacks which are inherent to the method itself. This visualization method is based on the interaction of an, otherwise, opaque sample with a specific type of radiation and, more specifically, with the attenuation of the radiation due to its absorbance from materials with different attenuation coefficients. Occasionally, there is a low contrast between distinct features, either belonging to different materials, or having spatial characteristics which are close to the resolution of the method itself. Such an example is the distinction between the solid matrix and an existing fracture which commonly has a very small aperture [14, 15, 16, 15, 17]. Consequently, a lot of effort has to be made to “clean” the acquired data from potential noise, independently of its source [18, 19, 20].

As a means to tackle such issues, there have been many studies focusing on the enhancement and optimization of digital image processing with the use of filtering methods [19, 21] which could reduce the inherent noise of the data while not harming the features of interest. With the help of filtering methods one can enhance the quality of the produced images by clearing unwanted artifacts. In such way “clean” images can be obtained with an enhanced contrast between the features of interest and their surroundings.

In the work of Poulouse et al. [22], the authors classified the available filtering methods. Their classification can be narrowed down into two major categories, namely the linear and the non-linear ones [23]. The latter type of filtering methods makes use of the intensities of the neighboring pixels in comparison to intensities of the ones of interest in an image, thus, updating the target pixel’s grayscale value accordingly (either increase or decrease it). There are two well-known filtering methods of this type; one is referred to as “anisotropic diffusion” [24], where a blurring scheme is applied in correlation with a threshold gray-scale value for the contrast between the target and the neighboring pixels.

The other method is referred to as the “non-local means filter” [25]. This method uses mean intensities to compute the variance (similarity) at the local area surrounding a target pixel in order to adjust the target pixel’s intensity in a way that the higher contrast (preferably at the edges of the features of interest) can be enhanced, while lower contrast (noise) can be smoothened. As an improvement to this filter, the “adaptive manifolds non-local means filter” [26] has been recently developed to reduce the data noise with the help of a Euclidean-geodesic relation between pixel intensities and calculated local mean intensities of the created manifolds on a higher dimension, since the grayscale value is accounted for as a separate dimension for each pixel.

On the other hand, the linear type of filtering methods makes use only of fixed (pixel-oriented) criteria. This, in practise, means that it simply blurs the image without distinguishing between generic noise and the boundaries of an object of interest. Some representative examples of such filters are the average and Gaussian filter, where the former updates a target pixel’s value with a mean value which is computed based on the adjacent pixels, and the latter utilizes a Gaussian shape function instead of a mean value.

Although there are no prerequisites in the selection of the appropriate noise filtering method, the non-linear type of filtering is more frequently employed with XRCT due to its edge conserving characteristic [27, 10, 28]. In other words, the outlines of the features of interest are maintained while noise is removed, or suppressed. Consequently, this can potentially help us to obtain a better signal-to-noise ratio in the acquired images which offers a great help to achieve a clear pixel-wise classification of image objects (segmentation).

Conventionally, segmentation can take place simply by applying a certain threshold to classify the image corresponding to pixel intensity. For instance, higher intensities than the adopted threshold are registered as logical true, while the remaining ones get registered as logical false. Since this threshold is chosen along the range of intensities within images, the choice of the threshold can be performed in a histogram domain, based on the assumption that similar features will most probably bear similar intensities. The most well-known approach based on this scheme is the “Otsu method” [29]. In this segmentation scheme histogram information of intensities is used so that the scheme returns a threshold value which classifies the pixels into two classes. The one is of interest and the other is out of interest by finding a maximum variance of inter-classes.

As an advanced intensity-based approach for multi-class applications, the K-mean method is also often used [30, 31, 32]. The K-mean method is an unsupervised clustering scheme which allocates data into predefined numbers of groups in a way that the variance within each group gets minimized [33]. In this way, in the work of Dhanachandra et al. [31], the authors showed their effectively segmented results of malaria-infected blood cells with the help of this method. However, this intensity-based segmentation approach could not be a general solution for XRCT data due to the “beam-hardening” effects, which creates imaging artifacts. These artifacts are caused by polychromatic X-rays (more than one wavelengths) which induce different attenuation rates along the thickness of different materials. For instance, among different energy profiles of X-rays, only the higher-energy X-ray would be able to pass over the thicker (inner) region of a sample, while both, higher and lower-energy X-rays, would be collected after crossing the thinner part (outer) [34]. Consequently, this makes the outer region of the object brighter and the inner region of the object

darker, which means that the histogram-based segmentation result could vary depending on the location of the region of interest in the acquired images.

As another common approach of segmentation, the methods based on “edge-detection” are also often adopted in image processing applications [30, 35]. In this scheme, unlike the above mentioned intensity-based methods, one could utilize the contrast of intensities within the images which would eventually outline the features of interest [36]. Based on the assumption that the biggest contrast would be detected where two differently gray-scaled features meet, there are many different types of operators in order to compute this contrast, namely Canny [37], Sobel [38] and Laplacian [39]. With these operators the contrast of a pixel is calculated in comparison to the neighboring pixels in each of x and y direction thus, the magnitude of the difference and the orientation could be obtained.

Since the method is relying on intensity local gradients, this scheme could be used to obtain the outline of the features independently of any beam-hardening effects.

However, despite the potential of this scheme, there is an inherent limitation to apply the method to XRCT applications. Since the method is designed to detect boundaries of features based on differences of intensities, preferably at the outlines of the features, the image has to have a high signal-to-noise ratio so that effective segmentation can take place resulting in clear boundaries. However, this condition can not be often matched with the tomographic images of fractures. This is mostly due to the physical size of fractures, which is close to the resolution of the imaging setup, casting the edges of the fracture blurry and not-so-easy to identify in terms of their boundaries.

In the field of medical imaging some methods were proposed in order to be applied to blood vessels imaging segmentation ([40, 41, 42], which also have a thin profile, as rock fractures do. These methods are using the Hessian matrix which is a matrix of second-order partial derivatives. In this case, the partial derivatives are computed for the intensities of an image pixel with respect to the adjacent pixels in each of x and y direction. Since second-order partial derivatives state changes of gradients with respect to the spatial degrees of freedom (directions), one could obtain a local shape at a specific pixel by computing the eigenvalues of the Hessian matrix. In the results of the above mentioned works, by applying this characteristic of a Hessian matrix, the authors were able to identify the structural information which corresponded to the shape of the blood vessels (tube-like shape). Consequently, they showed that a good segmentation could be performed with noisy and low contrast image data by utilizing the obtained structural information.

In the work of Voorn et al. [43], the authors adopted this Hessian matrix-based scheme and employed “Multi-scale Hessian Fracture” (MHF) filtering to enhance the narrow planar shape of fractures in 3D XRCT scanned data of rock samples. Before computing the Hessian matrix of the image, the authors applied a Gaussian filter to improve the visibility of the fractures. Since the improved features would differ corresponding to a chosen standard deviation of the Gaussian distribution-shaped function, which is used for the filtering, they applied various standard deviations in order to collect maximum responses from the Hessian matrix computation. This resulted in them being able to enhance the fractures of various apertures in their obtained XRCT images thus, they could easily binarize their images with the help of emphasized responses with structural information obtained from the Hessian matrix. This scheme was also employed in the work of Deng et al. [44]. They introduced the “Technique of Iterative Local Thresholding” (TILT) in order to segment a single fracture in their rock images. After acquiring an initial image just to get a rough shape of the fracture by using a threshold or MHF, they applied the *Local threshold* method ([45]), which sets a threshold individually for every pixel (See. 2.3.1), repeatedly to narrow down the rough shape into a finer one until its boundary reaches the outline of the fracture.

Despite the successful segmentation of their data-set, some challenges still remained for the segmentation for fracture network applications, as expressed in the work of Drechsler et al. [46]. The authors compared the famous Hessian-based algorithms with each other such as namely Sato, Frangi and Erdt. In their study they showed that these schemes are not too effective to classify the intersections of the features of interest. This was because the Hessian matrix-based schemes mostly enhance the one directional (long and thin in one direction in a 2D case) shape while the intersections are multi-directional. This is commonly considered as a plane (no features) in this scheme. Additionally, in the case of MHF, due to the used Gaussian filter, which blurs the edges of a fracture, the surface roughness of fractures will most probably not be identified. Also, the segmentation results varied significantly corresponding to the chosen range of standard deviations [44].

These properties make the Hessian-based methods less effective for fracture network segmentation, which often contains a significant number of crossing areas and a certain roughness at the fracture surface. The same problem is also met in the TILT method. Since the results of the method strongly depend on the initially binarized image, the method is commonly not able to deal with a not-so-clear initial image which does not cover the intersection reasonably.

As a more advanced segmentation approach, the watershed segmentation method was introduced by Beucher and Meyer [47]. The main difference of this segmentation method from the others is that this method is performed in a label-wise manner. This practically means that one could obtain individually assigned groups of pixels (features) as a segmentation

result. This can be accomplished by following the following steps: 1. One should find the local intensity minimums for each one of the assigned groups of pixels. 2. At each local minimum, the assignment of the nearby pixels to individual label groups is performed according to the magnitudes of the corresponding intensity gradients. During this assignment, the pixels with the lower gradients should be included into the same group preferentially. Also, a distance map, where the distance is computed from all non-zero pixels of a binarized image, could be used instead of an image which contains intensity values [48]. 3. The above mentioned procedures ought to be performed repetitively until there are no more pixels to be assigned (until the boundaries are reached, where the gradients should take their maximum value). In the work of Taylor et al. [10], based on the watershed method, they were able to successfully visualize a segmented void space of XRCT scanned sand which also had the shape of a narrow region, similar to fractures.

In the work of Ramandi et al. [28], the authors demonstrated the segmentation result of coal cleats by applying a more advanced scheme based on the watershed method, the Converging Active Contour (CAC) method, initially developed by Sheppard et al. [27]. Their method combined two different schemes; one was the watershed method itself, and the other was the active contouring method [49], which is commonly used for finding the continuous and compact outline of the features from an, initial, binary image. This could be done with the minimization of a two-term energy function, with one term consisting of the curvature and length of the outline, and the other term being the desired feature, by using intensity gradients of the original image. Consequently, the outline of the initial binary image would be deformed at the locations of higher gradients (mostly edges of the features). With the help of this idea and the watershed method, by inspecting the intensity histogram of their data they carefully chose threshold values to group the pixels into three different groups such as void, solid and unallocated. In their scheme, as watershed algorithm does, they assigned the unallocated pixels into void and solid groups according to their intensity gradient. Consequently, the contours of each of the groups expanded until the two outlines meet. However, there was still a fundamental limitation to cope with, to directly segment a fracture with the introduced method since the method requires a well-selected initial group of pixels, while it is hard to define those only with a threshold due to the low contrast of the feature [9]. In the work of the same authors [28], in order to overcome this issue, they applied a saturation technique with an X-ray attenuating fluid which was a mixture of Sodium Iodide (NaI) and Potassium Chloride (KCL). By performing this they were able to enhance the visibility of the pores and fractures within their XRCT data. They stated that this saturation prerequisite, which included intrusion and pressurization, took 8 days to be complete.

By considering this effort to enhance the visibility, a segmentation method which could cope with a dry fracture without additional extensive effort and time would be desirable to boost the identification of fractured specimens via image processing. However, this is very hard to be achieved with a conventionally designed segmentation method due to the above mentioned issues. More specifically, since the shape of natural fractures is often too sophisticated while having a low contrast of intensities in its scanned data, it is difficult to find a well-performing segmentation method while still having to deal with inherent defects of the XRCT data such as noise, artifacts, and beam-hardening effects.

Instead of dealing with the image with numerically designed schemes, in recent years and in various fields like remote sensing [50], medical imaging [51] and computer vision [52], image segmentation using machine learning techniques has been being robustly studied as a new approach due to its well-known benefits, like flexibility to all types of applications and less demanding user intervention.

In a machine learning scheme, a model is designed to be able to identify a pattern from given data, thus, ultimately, performing a task as a human would. For instance, with given input and annotated data (truth), where the annotation is often evaluated and performed by an operator, a model is mapping the relation between these two by updating its inner coefficients. The updating is done in a way that the model narrows down the differences between the input and annotated data (training). Consequently, when the gap is sufficiently reduced, the model is able to perform the same task so that it builds the ability to predict the desired output (prediction) for a new input data based on the training. This workflow makes a machine learning scheme convenient for most of applications, since it does not require an explicitly considered numerical scheme for a purpose.

Based on this advantage, in the work of Kodym et al. [53], the authors showed a semi-automatic image segmentation workflow with XRCT data by using the Random Forest algorithm [54] which statistically evaluated the outputs from decision trees (See 2.4). With the help of this algorithm, by providing a few manually annotated as truth images to the model, the authors were able to obtain the segmented result from arbitrary tissues in 3D medical CT data, regardless of the intensities or the edges, as long as some detected characteristics of the object were contained in the manually annotated truth.

In the work of Karimpouli et al. [3], the authors demonstrated cleats segmentation results from CT scanned coal sample data by applying the Convolutional Neural Networks CNN approach, which is another type of a machine learning scheme. The CNN is one of the deep artificial neural network models which consists of multi-layers with convolutional and max-pooling layers [55]. The former layer is employed to extract features out of an input image and the latter one is employed to down-sample the input by collecting the maximum coefficients which are obtained

from the convolutional layers. With the help of a combination of these layers, an input image could be narrowed down into a binary classification, while capturing the important information. In their work, the model was able to classify a center-placed voxel whether it belonged to a fracture or not, within a given small size ( $19 \times 19$  voxels) of an input image after training the model with manually annotated truth. By performing this procedure recursively for every pixel within the scanned image and combining, a fully segmented image was able to be obtained.

Based on CNNs architecture, in the work of Long et al. [56], the authors demonstrated the Fully Convolutional Networks FCNs model, which is a more advanced model. Unlike CNN, instead of dragging down an image to a pixel for classification, the model has the ability to classify the image in a pixel-wise manner, which means that a classified image could be obtained as an output of the model. The model consists of an encoding part, which is of the same structure as the CNNs, and a decoding part, which up-samples the layers using a deconvolutional operation (See 2.5). The authors also introduced a skip connection scheme, which is concatenating the previously maximum collected layers into the decoding part in order to enhance the prediction of the model. This is to compensate for the data loss during the down/up-sampling, since some details would be lost during the pooling operation. Thus, it was beneficial to locate the pixels of prediction by using this skip connection scheme since the accumulated details from previous layers would also be used for the up-sampling.

In the work of Furat et al. [17], the authors presented their segmentation results of thin grain boundaries with Al-5 wt.% Cu alloy. These grain boundaries were induced by Ostwald ripening [57] after heating up and annealing the specimen. The grains separated from the liquid alloy get coarser during the annealing period. In order to identify the growing grains due to ripening, they scanned the sample during each different stage by means of XRCT so that the initial scan contained more liquid phase than the other scans, while the sample at the end stage had mostly coagulated grains. They applied the famous U-net model [58], to obtain the grain boundaries, which is one type of CNNs with nearly the same structure as FCNs. A truth data-set in order to train the model was obtained at the final stage by means of 3D X-ray Diffraction 3DXRD which provided the information of orientation, size and shape of the grains within a sample [59]. By training their model in this manner, they were able to achieve the segmented rough grain boundaries. Some conventional segmentation means, such as the watershed method, were employed based on this initial result to get clear grain boundaries.

Despite these promising results from the use of a machine learning scheme there is still room for improvement. In a machine learning based scheme, apart from improving the architecture of the training model which significantly affects the efficiency and output of the model [60], one major issue is how we can provide a truth data. In most applications [61, 62, 63, 64], this was performed based on subjective manual annotation which would consume noticeable time and effort of an expert. This manual annotation is hardly the best approach, especially in our application which contains sophisticated shapes of fracture networks and low contrast features due to the low density of air within the small volume of a fracture. Although in the work of Furat et al. the authors cleverly provided the truth data by means of 3DXRD, this approach requires additional scans and even the facilities to perform the process properly.

By taking into consideration that a machine learning scheme has the potential to perform segmentation with only few truth data, it may be easier to obtain some truth data by means of conventional segmentation for training the model than carrying out manual annotation or additional scanning. Specifically, although there were some successful cases in the previously mentioned works, most of these works were target-oriented and designed for their own application, thus, it was hard to generalize their algorithms so as to be applicable to other objectives. In addition, it is often the case that one should spend a lot of time tuning the parameters of the conventional methods due to different features in each of the images. Since the conventional methods mostly rely on fixed criteria, it is hard to be flexible enough to deal with this type of variation within the data. Nevertheless, the above mentioned works with conventional segmentation methods indicate us that there are some effective methods to deal with the fracture application. Additionally, finding a parameter for a partial data-set does not require much effort and computation time as manual annotation does. Therefore, it would be beneficial that one utilized the conventional segmented result from a partial data-set, where it is easy to obtain a good quality of segmentation as the ground truth, in a machine learning scheme.

Based on this idea, in this article we focus on the efficient workflow of segmentation in order to obtain the complete 3D structure of a dry fracture network scanned with XRCT. The 3D structure is obtained by stacking the 2D processed results. The fracture network is induced by thermal quenching of Carrara marble, which creates a sophisticated shape of fracture network within a reasonably homogeneous and fine-grained matrix.

For comparative purposes, three different combinations of segmentation techniques were adopted based on conventional means such as the Sato, Local threshold, and active contouring method, including filtering and post-processing. Two different machine learning models were employed for this comparison as well. The well-known U-net ([58]), as well as the Random forest model, were evaluated, with the Random forest model being supported in Trainable Weka ([65]).

We adopted the 2D U-net model in this study which could only deal with 2D data since the 3D model ([17]) would compromise our computational ability. However, even for the adopted 2D model we reached memory limitations with a slice of image. Thus, we had to dice the 2D images into small 2D tiles and compute sequentially. These computed prediction tiles were merged together at a later step to shape the 2D image. In order to train the adopted model, we provided a training data which was obtained by means of a conventional segmentation method. Note that only a small portion of the results (60 slices out of 2140 images) was used as a training data-set. In this way, although it was also memory-wise possible to run 3D model by separating the volume into extremely small ones, this was not conducted in this study since the volume size was not sufficient to contain useful information. For a fair comparison between methods, all segmentation schemes were applied on 2D data.

Via comparison, we were able to identify that the U-net segmentation model outperformed the others in terms of quality of the output and time efficiency. Some defects which appeared in the provided truth data by conventional segmentation means were smeared out in the predictions of the model.

## 2 Materials and methods

### 2.1 Data acquisition and sample preparation

The segmentation approach presented in this paper is based on a  $\mu$ XRCT data set of a thermally treated Bianco Carrara marble core sample. The data set along with all meta data can be found in [66]. Bianco Carrara marble is a crystalline rock, consisting of about 98 % calcite ( $\text{CaCO}_3$ ) [67]. It is a frequently used material in experimental rock mechanics since it combines several aspects, such as high mineral purity, very low porosity as well as almost homogeneous and isotropic behavior on the macro scale, casting it to a very reproducible material for experimental investigations, cf. [68]. In combination with mechanical or thermal treatments, the virgin state can be modified to achieve different micro-fracture characteristics within the sample. By varying the parameters of a thermal treatment, for instance, the crack density and the mean crack aspect-ratio can be influenced, cf. [69, 70]. This allows the experimental study of different physical phenomena related to micro-fractures and micro-fracture networks like, for instance, the influence on the wave propagation [69], the change of elastic and electrical properties [70], the stress-dependent permeability and wave dispersion in presence of micro-cracks [71, 68] or the experimental verification of Hudson's theory [72].

The scanned cylindrical core sample was extracted from a thermally treated bigger cylindrical core sample with a diameter of 30 mm and a length of 80 mm. The applied thermal treatment consisted of the following steps: 1. heating-up from room temperature ( $20^\circ\text{C}$ ) to  $600^\circ\text{C}$  with a heating rate of  $3\text{ K min}^{-1}$ . 2. holding this temperature for 2 h to ensure a uniform temperature distribution in the entire sample. 3. quenching the sample in a water basin at room temperature ( $20^\circ\text{C}$ ). Since the resulting crack apertures are expected to be in the range of a few micrometers, it is crucial to extract a small enough sample for the  $\mu$ XRCT scan to improve the resolution of these small features. For this, a cylindrical sample (diameter 5 mm; length 10 mm) was extracted using a water-cooled diamond drill and saw.

The scan of the extracted sample was performed in an in-house developed, modular cone-beam  $\mu$ XRCT system. As X-ray source and detector, the open micro-focus tube *FineTec FORE 180.01C TT* with a tungsten transmission target from Finetec Technologies GmbH, Germany in combination with the *Shad-o-Box 6K HS* detector with a CsI scintillator option from Teledyne DALSA Inc., Waterloo, Ontario, Canada were employed. The latter provides a resolution of  $2940 \times 2304$  pixels by a pixel pitch of  $49.5\ \mu\text{m}$  and 14-bit depth resolution. For more details about the system please refer to [73]. The highest achievable spatial resolution with this system is about 50 line-pairs/mm at 10 % of Modulation Transfer Function (MTF) which is equal to a resolvable feature size of about  $10\ \mu\text{m}$ . To achieve this, we used a geometric magnification of 24.76 resulting in a voxel size of  $2.0\ \mu\text{m}$ . With these settings, the corresponding Field Of View (FOV) was 5.88 mm in the horizontal direction and 4.61 mm in the vertical one. Consequently, the sample could be scanned over the entire diameter of 5 mm.

For further details about the image acquisition settings cf. [66, 73] and . The reconstruction was performed using the Filtered Back Projection (FBP) method implemented in the software *Octopus Reconstruction (Version 8.9.4-64 bit)*. The reconstructed 3D volume consists of  $2940 \times 2940 \times 2139$  voxels, saved as an image stack of 2139 16-bit \*.tif image files of  $2940 \times 2940$  resolution. Noise reduction was deliberately omitted in the reconstruction process in order to provide an interested reader with the possibility to use their own adequate noise filtering methods. The 3D data set with an extraction to better show the homogeneous fracture network is illustrated in Figure 1. The bright gray area represents the calcite phase whereas the dark gray area in between the calcite phase shows the initiated micro-fractures which were generated by the thermal treatment. As a consequence of the thermal treatment, a bulk volume increase of about 3.0 % under ambient conditions can be recorded if a perfect cylindrical sample shape is assumed. The porosity of the underlying raw material is about 0.57 % measured with mercury porosimetry.

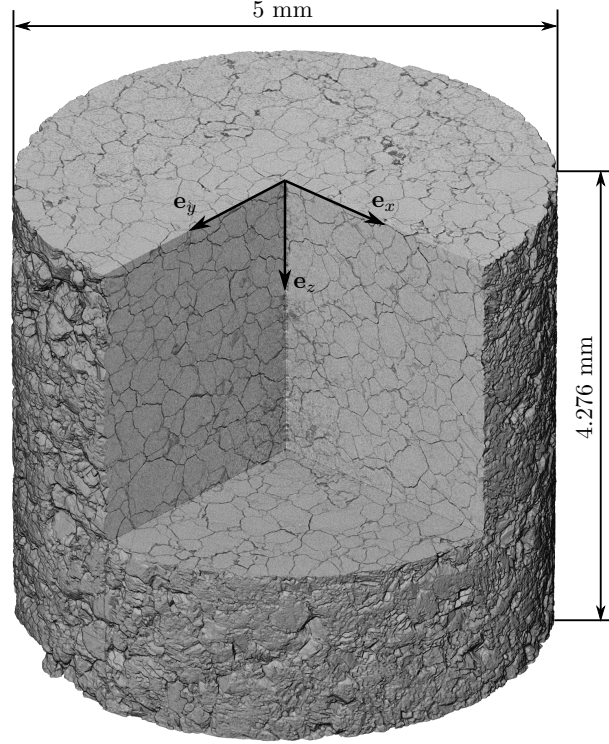


Figure 1: Illustration of the underlying raw  $\mu$ XRCT dataset of a thermally treated Bianco Carrara marble sample taken from [73]. The dataset along with all meta data can be found in [66], <https://doi.org/10.18419/darus-682>; licensed under a Creative Commons Attribution (CC BY) license.

## 2.2 Noise reduction

Applying a digital filtering method to reduce the noise of the obtained images is a common approach to enhance the quality of the image itself, and further segmentation [21]. However, it is also often found that a filter can blur the features of interest while smoothing out noise in the images. For our application, in order to conserve the edges information while reducing artifacts, the Adaptive Manifolds Non-Local Mean (AMNLM) method [26] was adopted. As shown in fig. 2, this procedure was an essential step to obtain good segmentation results with some of the conventional segmentation methods. The adopted filtering method was applied with the help of the commercial software Avizo (2019.02 ver) (<https://www.fei.com/software/amira-avizo>). The numerical description of this filtering method in 2D is explained in this chapter. For the better understanding, we adopted modified notations in the work of Gastal et al. [26].

The AMNLM filter operates in two parts : 1.) creation of matrices (manifolds) which are filled with weighted intensities by coefficients. 2.) iterative processing on created matrices. In the first part, in order to reduce the complexity and increase the efficiency of the filter, Gastal et al. introduced the Principal Component Analysis (PCA) (Pearson1901) scheme on the created matrices. In the second part, sequential steps were presented to adjust intensities of pixels based on components of created and PCA treated matrices. These procedures are called *Splating*, *Blurring* and *Slicing*. The *Splating* and *Blurring* are iterative steps on components of created matrices with numerical modifications (adaptive manifolds). After these iterative procedures, *Slicing* is performed which is merely summing the outputs from the iteration and normalizing it.

From the creation of manifolds the coefficients to weight intensities were designed to have a shape of a Gaussian distribution in the kernel. A typical two-dimensional isotropic Gaussian kernel can be derived as follows,

$$G((x, y); \sigma_f) = A \exp\left(-\frac{x^2 + y^2}{2\sigma_f^2}\right) \quad (1)$$

where  $A$  is an arbitrary chosen amplitude of the Gaussian profile,  $x$  and  $y$  are input vectors which have a mean value of zero, and  $\sigma_f$  is the standard deviation of Gaussian distribution.

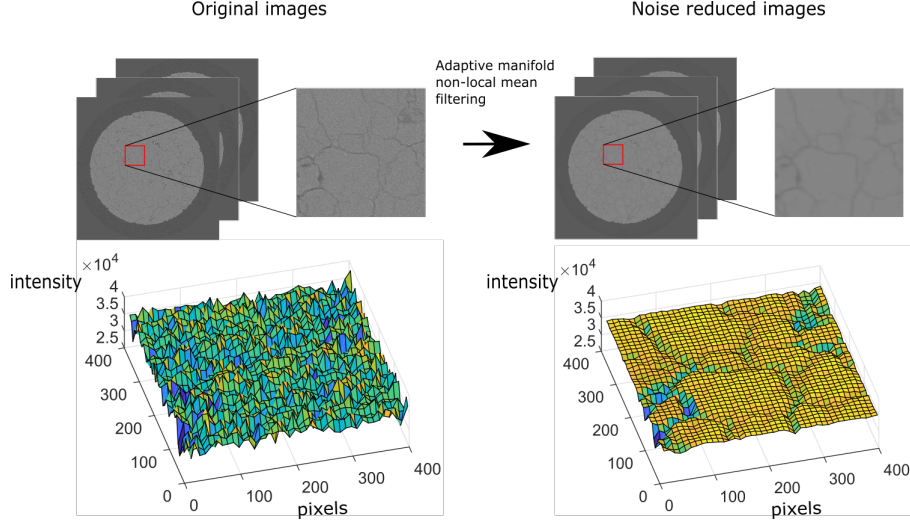


Figure 2: Effect of filtering. The images shown at the above are 2D images of original image (left side) and noise reduced image (right side) by applying 3D adaptive manifolds non-local mean filtering [26]. The red box areas are zoomed (400 x 400 pixels). At the below, intensity surfaces of both images at the zoomed domain is shown.

By using the above profile and input vectors, a finite sized Gaussian kernel  $G_k$  could be defined. With the created Gaussian kernel, the manifolds of weighted intensities  $f_A$  could be created as follows,

$$f_A = \text{vec}(G_k)^T \cdot \text{vec}(I) \quad (2)$$

where  $\text{vec}(\cdot)$  is a vectorization operator and  $I$  is the 2D image matrix which contains intensities.

Each dimension of  $f_A$  contains weighted intensities from the image. The dimensionality of the PCA scheme was reduced in order to boost the computation efficiency while minimizing the loss of information [74]. This could be achieved by finding the principal components which would maximize the variance of data in dimensions of  $f_A$ . The principal components could be obtained by computing eigenvalues and their corresponding eigenvectors of covariance matrix  $C$ . The covariance matrix  $C$  of  $f_A$  is acquired as follows,

$$C = (f_A - \mathcal{E}(f_A))^T (f_A - \mathcal{E}(f_A)) \quad (3)$$

where  $\mathcal{E}$  operator is to compute means of its arguments.

Among the eigenvalues of the obtained  $C$ , the bigger ones indicate higher variances of the data in the corresponding eigenvector space [74]. Thus, after sorting the corresponding eigenvectors in an order of magnitudes of eigenvalues, by performing multiplication with these eigenvectors and  $f_A$ , the manifolds  $f_A$  could be ordered in order of significance. Based on this, the user defined number of dimensionality  $s$  is adopted and the manifold  $f_A$  is recast into  $f_S$  by extracting  $s$  number of principal components.

**Splatting** With the given extracted manifolds  $f_S$ , the Gaussian distance-weighted projection is performed as follows,

$$\Psi_0 = \exp \left( - \frac{\sum_{i=1}^S |f_i - \eta_i|^2}{2\sigma_r^2} \right), \quad (4)$$

with  $\Psi_p$  being the coefficients to weight the original image (projection),  $\sigma_r$  being a chosen filtering parameter which states the standard deviation of filter range, and  $\eta_S$  denoting the *Adaptive manifolds* which are noise reduced responses by a low-pass filter (See eq. 5) at the first iteration. These adaptive manifolds will be further updated via an iteration process. Consequently, the Euclidean distances between each of  $f_S$  and  $\eta_S$  are computed and integrated into  $\Psi_0$  by considering the standard deviation  $\sigma_r$ .

In order to obtain *Adaptive manifolds*, the numerical description of the low-pass filter for a 1-D signal in the work of Gastal et al. [26] is as follows,

$$S_{out}[i] = S_{in}[i] + \exp \left( - \frac{\sqrt{2}}{\sigma_s} \right) (S_{in}[i-1] - S_{in}[i]), \quad (5)$$

where  $S_{out}$  is the response of the filter,  $S_{in}$  is the signal input, and  $\sigma_s$  is a filtering parameter which states the spatial standard deviation of the filter.  $i$  denotes the location of a pixel in the image. Note that this low-pass filter has to be applied to each direction in an image due to its non-symmetric response corresponding to the applied direction. With this relation, the collected response has a smoother profile than the original signal.

By performing element-wise multiplication on the acquired  $\Psi_p$  and the original image  $I$ , the weighted image  $\Psi$  could be obtained such as,

$$\Psi = \Psi_0 \circ I. \quad (6)$$

where  $\circ$  denotes the Schur product ([75]).

**Blurring** In the computed weighted image  $\Psi$  and the *adaptive manifolds*  $\eta_S$ , Recursive Filtering (RF) [76] is applied so that the values of each manifold in  $\eta_S$  can be blurred accordingly in  $\Psi$  and  $\Psi_0$ . Gastal et al. proposed to conduct this procedure in a down-scaled domain so that further smoothing could be expected after the following up-scaling interpolation. The down-scaling factor  $d_f$  is calculated as such (e.g.,  $d_f = 2$  states a half-scaled domain),

$$d_f = \max(1, 2 \lfloor \log_2(\min(\sigma_s/4, 256 \sigma_r)) \rfloor). \quad (7)$$

by taking into account the adopted spatial/intensity filter range of standard deviations  $\sigma_s$  and  $\sigma_r$ .

**Slicing** As mentioned above, the *Splating* and *Blurring* steps are performed in an iterative manner and, at each iteration step, a weight projection matrix  $\Psi_0$  and a weighted image  $\Psi$  are created. By defining the *Blurring* responses of these with RF as  $\Psi^{blur}(k)$  and  $\Psi_0^{blur}(k)$  where  $k$  represents iteration number, the final normalized result of the filter  $I_f$  is as follows,

$$I_f = \frac{\sum_{k=1}^K \Psi^{blur}(k) \circ \Psi_0(k)}{\sum_{k=1}^K \Psi_0^{blur}(k) \circ \Psi_0(k)} \quad (8)$$

where  $K$  is the total numbers of created adaptive manifolds. Note that up-scaling is performed by bilinear interpolation on every  $\Psi^{blur}$  and  $\Psi_0^{blur}$  to recover the domain size from the down-scaled one due to *Blurring* step.

**Adaptive manifolds** In the first iteration, the  $\eta_S$  are obtained from the low-pass filter response of  $f_S$  with the use of Eq. 5. The responses of the low-pass filter locally represent the mean value of the local intensities, which reflects well the majority of intensities within the sub-domain while it lacks variation. By taking into account this drawback, Gastal et al. introduced a hierarchical structure to include better representative information from additionally created dimensions. These additional dimensions are created by clustering the pixels of  $f_S$ . By taking each of  $\eta_S$  as default points, the pixels which had intensities above  $\eta_S$  and below are classified accordingly.

This type of clustering, i.e. finding which pixels are located above and below  $\eta_S$ , could be acquired by the eigenvalues of the covariance matrix of  $(f_S - \eta_S)$  with eq. 3. From the dot product of the obtained eigenvalues and  $(f_S - \eta_S)$ , the clustered pixels are,

$$\begin{cases} p_i \in C_-, & \text{if } J < 0, \\ p_i \in C_+, & \text{otherwise,} \end{cases} \quad (9)$$

where  $J$  is the dot product,  $p_i$  is pixel  $i$ ,  $C_-$  and  $C_+$  denote the clusters with pixels below and above the manifold, respectively.

Based on the computed clusters  $C_-$  and  $C_+$ , *Adaptive manifolds* are calculated as follows,

$$\eta_{S-} = \mathcal{L}_p(C_- \circ (1 - \Psi_0) \circ f_S, \sigma_s) \oslash \mathcal{L}_p(C_- \circ (1 - \Psi_0), \sigma_s), \quad (10)$$

and

$$\eta_{S+} = \mathcal{L}_p(C_+ \circ (1 - \Psi_0) \circ f_S, \sigma_s) \oslash \mathcal{L}_p(C_+ \circ (1 - \Psi_0), \sigma_s), \quad (11)$$

where  $\mathcal{L}_p$  indicates the low-pass filter in eq. 5 and  $\oslash$  is an element-wise division operator (referecne, Wetzstein, Gordon). Note that the low-pass filter is performed on down-scaled domain such as the step in *Blurring*. Thus, in order to match the size of matrix,  $\eta_S$  is up-scaled before it is applied to *Splating* step. These steps are performed iteratively (See eq. 8). Thus,  $K = 2^h - 1$  numbers of manifold are created while  $h$  is defined as follows,

$$h = 2 + \max(2, \lceil (\lfloor \log_2 \sigma_s \rfloor - 1)(1 - \sigma_r) \rceil). \quad (12)$$

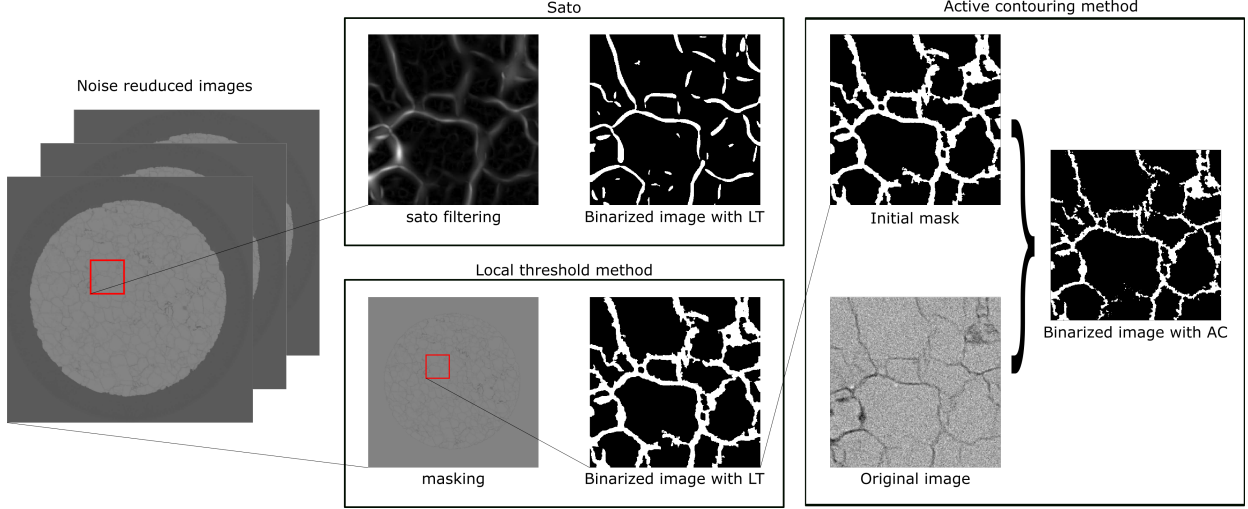


Figure 3: Workflows of adopted conventional methods: The workflows of segmentation with Sato, Local threshold (LT) method and Active contouring AC method are shown with obtained images from each step. The magnified region is marked with red color.

## 2.3 Segmentation methods

The adopted segmentation methods in our application are introduced in this chapter. As conventional schemes, Local threshold, Sato and Active contouring methods are chosen in order to obtain fine segmentation results. The U-net and Random Forest Decision Tree models are used by means of segmentation based on machine learning algorithms (See. fig. 4). Note that the adopted conventional segmentation methods had to be employed with noise-reduced images and also required certain workflows (See. fig 3). The workflow of machine learning based algorithm is also described in fig. 4).

### 2.3.1 The Local Threshold method

The *Local Threshold* method is a binarization method, also known as the adaptive threshold method. Unlike a common threshold method, which merely sets up a global threshold value which could be applied on the entire domain of an image, one can create a threshold map which has the same size as this of the input image for binarization, corresponding to the intensities within the local region. This could be done by acquiring a smoothed image (weighted mean) within a local region which takes into account the intensities of the adjacent pixels, subtracting an offset from this smoothed image. The choice of this offset can vary depending on the intensities of the original image however, should be performed to contain the feature of interest within the final binarized image. The output of the above mentioned procedure is a map which includes individual thresholds (local threshold) for each pixel. From the obtained threshold map, the binarization is performed by setting the pixels which contain higher intensities than the corresponding location at the threshold map as logical truth, and the others to be logical false.

For our application, this method was applied on noise reduced data in order to minimize the affects of artifacts. Smoothing was performed in order to obtain a threshold map with the help of Gaussian filtering Eq. 13. Parameters like the offset and the radius of adjacent area were empirically selected. This procedure was performed with the *threshold\_local* function in python *skimage* library. Small artifacts which remained, despite of the adopted segmentation method and the noise reduction technique, were removed by employing the *remove\_small\_object* function from the same library.

Since the method creates the threshold map which considers the contrast between adjacent pixels, the method is not affected by spatially-varying intensity gradients. However, due to the fact that the method works by capturing highest contrast from weighted neighboring pixels, it can not effectively perform the segmentation when two different contrast exist (one is bigger than the other). In this case, only bigger contrast will be considered. Specifically, in our application, the fractures close to the outer rim of the sample could not be segmented well with this method, since the contrast between the sample and its environment was much larger than the contrast between the fracture and the grains. In order to cope with this problem, before applying the method another step was necessary, the filling of the outer part with a

mean intensity value extracted from a region of the image where a fracture was not contained. Consequently, the larger contrast between the outer rim and the sample could be eliminated.

### 2.3.2 The Sato method

The *Sato* filtering method proposed by [40] is one of the most well-known filtering methods in the field of medical image processing, and it was initially applied on the segmentation of blood vessels. The potential of this filter in finding structural information is well matching for the segmentation of a fracture, which often has a long and thin string-like shape in two-dimensional images.

The filter consists of two fundamental parts: a Gaussian filter and a Hessian matrix. In the Gaussian filtering part, with the Gaussian shape profile in eq.1, a finite-sized kernel  $w$  is designed by defining the input vectors  $(x, y) = [-l_w, l_w]$  with a mean value of zero, and  $l_w$  being a positive integer defined by the standard deviation  $\sigma_f$  and truncate factor  $t_f$  ( $l_w = (t_f == 4) * \sigma_f + 0.5$ ). For the sake of stability of the kernel behavior, the kernel is normalized by dividing with the sum of all of its elements. Finally, the Gaussian filter can be expressed by means of the kernel with a convolution operator  $\otimes$  such as,

$$I_f(\mathbf{X}) = G(w(x, y); \sigma_f) \otimes I(\mathbf{X}), \quad (13)$$

where  $I$  is an intensity matrix (input image). in the spatial domain  $\mathbf{X}$  and  $I_f$  being Gaussian-filtered image.

The Hessian matrix is a matrix of second order partial derivatives of intensities in the  $x$  and  $y$  directions, and is often used to trace local curvatures with its eigenvalues. By bringing this concept to an image we can deduce a local shape at selected pixels, while observing the changes of intensity gradients. The numerical description of a Hessian matrix with a Gaussian filtered image at selected pixel positions  $z$  is as follows,

$$\nabla^2 I_f(z) = \begin{bmatrix} \frac{\partial^2}{\partial x^2} I_f(z) & \frac{\partial^2}{\partial x \partial y} I_f(z) \\ \frac{\partial^2}{\partial y \partial x} I_f(z) & \frac{\partial^2}{\partial y^2} I_f(z) \end{bmatrix} \quad (14)$$

With eq. 13 we can re-write the elements of the matrix as the convolution of the input image and the second partial derivatives of the Gaussian shape function. For example, the first element of the Hessian matrix is,

$$\frac{\partial^2}{\partial x^2} I_f(z) = \frac{\partial^2}{\partial x^2} G(w(x, y); \sigma_f) \otimes I(z_w) \quad (15)$$

where  $z_w$  is the kernel which has its center at  $z$  and the same size as  $G$ . In this way we obtain a scalar element by convolution. Note that the second derivatives of the Gaussian shape function are conventionally used for reducing the noise while reinforcing the response of the signal with a specific standard deviation (in this case  $\sigma_f$ ) [43]. Thus, the elements in eq. 15 represent an enhanced intensity response of the aperture of the fracture in the original input image.

Defining the local structure at pixel  $z$  with the help of second order partial derivatives could be done by calculating the eigenvalues of the obtained Hessian matrix. In this case, since  $\frac{\partial^2}{\partial x \partial y} I_f$  and  $\frac{\partial^2}{\partial y \partial x} I_f$  are identical, the matrix is symmetric with real numbers thus, the eigenvalues of the matrix can be assured to be real numbers and its eigenvectors have to be orthogonal [77].

By defining the eigenvalues as  $\lambda_1$  and  $\lambda_2$ , the line-like shape curvature have a relation of  $|\lambda_1| \approx 0, |\lambda_2| \gg 0$  or vice versa. This is because each eigenvalue states an amount of gradient change at the selected pixel to each eigenvector direction (orthogonal when  $\lambda_1 \neq \lambda_2$ ). Then, in the case of line-like shape (long and thin), one must have a very small value of  $|\lambda_1|$  while the other has relatively bigger value of  $|\lambda_2|$ . The author proposed to replace the intensity value at pixel  $z$  to  $|\lambda_2|$  under the above mentioned line-like shape condition and to zero otherwise. Finally, the maximum responses from the output images were accumulated in a range of different  $\sigma_f$  to maximize the effects for various fracture apertures.

Based on this scheme, the multi-scaled Sato filtering method was applied on the noise reduced data with the *sato* function from python *skimage* library. Since the output of this method is an enhanced response of a string-like shape while minimizing the responses from the other shapes of structures, a further binarization method has to be applied to the output of the Sato method in order to obtain logical type of results. Here, we adopted the local threshold method (see 2.3.1) which was able to effectively distinguish the enhanced responses out of the output. As we mentioned in 2.3.1, before applying the binarization method, the outer part of the scanned data was eliminated since the contrast between the outer and inner part is bigger than the contrast of the fractures in the data.

After applying the binarization scheme, the remaining artifacts were eliminated with the use of morphological schemes such as *erosion* and *remove\_small\_object* which are also supported in the python *skimage* library.

### 2.3.3 The Active contouring method

In image processing, the active contouring method is one of the conventional methods applied in order to detect, smoothen, and clear the boundaries of the features of interest [49]. Instead of the conventional active contouring approach, which requires distinguishable gradient information within an image, we adopted the Chan-veese method [78] which makes use of the intensity information. This has an advantage especially for XRCT applications, as in this case, which contain low signal-to-noise ratio data due to the inherent noise which can potentially induce some inaccuracy in the segmentation.

By employing the method which was introduced in the work of Chan et al., we were able to obtain finer profiles from the segmented images. The method requires an initial mask which is a roughly segmented binary image and preferably contains most of the features of interest. Thus, we adopted the result of LT (See. 2.3.1) as the initial mask. From the given initial mask and the corresponding original image, we proceeded with the method to obtain a segmented image. This could be done by minimizing the differences between the mean intensities of in-/out areas, defined by the boundaries of the initial mask  $C$ , and the intensities from the original images  $I(x, y)$  based on a modified version of the *Mumford-Shah* functional [79],

$$F(c_1, c_2, C) = \mu L(C) + \nu A(in(C)) + \lambda_1 \int_{in(C)} |I(x, y) - c_1|^2 dx dy + \lambda_2 \int_{out(C)} |I(x, y) - c_2|^2 dx dy, \quad (16)$$

where  $F$  is the functional of  $c_1$  and  $c_2$  which are the average intensities within the region of in-/outside of  $C$ , and  $L$  is the length and  $A$  is the inside area of  $C$ . The  $\mu, \nu, \lambda_1$  and  $\lambda_2$  are input parameters.

In order to derive the numerical description within the common domain  $(x, y) \in \Omega$ , the level set scheme, which is able to describe the boundaries of a feature of interest and its area by introducing higher dimensional manifold [80], was combined in this relation. By following this scheme, the boundaries of the initial mask  $C$  and inner-/outer areas of it can be defined such as,

$$\begin{cases} C : \Phi(x, y) = 0 \\ in(C) : \Phi(x, y) > 0 \\ out(C) : \Phi(x, y) < 0, \end{cases} \quad (17)$$

where  $\Phi(x, y)$  is a Lipschitz continuous function to assure that it has a unique solution for a given case.

With the help of the scheme and a Heavyside step function  $H$ , eq. 16 could be rewritten within the common domain  $\Omega$  as follows,

$$\begin{aligned} F(c_1, c_2, \Phi) = & \mu \int_{\Omega} |\nabla H(\Phi(x, y))| dx dy + \nu \int_{\Omega} H(\Phi(x, y)) dx dy \\ & + \lambda_1 \int_{\Omega} |I(x, y) - c_1|^2 H(\Phi(x, y)) dx dy + \lambda_2 \int_{\Omega} |I(x, y) - c_2|^2 (1 - H(\Phi(x, y))) dx dy \end{aligned} \quad (18)$$

For the fixed  $\Phi$ , the intensity averages of interior  $c_1$  and exterior  $c_2$  of the contour could be obtained such as,

$$c_1(\Phi) = \frac{\int_{\Omega} I(x, y) H(\Phi(x, y)) dx dy}{\int_{\Omega} H(\Phi(x, y)) dx dy} \quad (19)$$

$$c_2(\Phi) = \frac{\int_{\Omega} I(x, y) (1 - H(\Phi(x, y))) dx dy}{\int_{\Omega} (1 - H(\Phi(x, y))) dx dy} \quad (20)$$

Based on these relations, in order to minimize  $F$ , the authors used the following scheme by relating it with an Euler-Lagrange equation. By applying the artificial time  $t \geq 0$ , the descending direction of  $\Phi$  is such as,

$$\frac{\partial \Phi}{\partial t} = \delta(\Phi) \left[ \mu \operatorname{div} \left( \frac{\nabla \Phi}{|\nabla \Phi|} \right) - \nu - \lambda_1 (I(x, y) - c_1)^2 + \lambda_2 (I(x, y) - c_2)^2 \right] \quad (21)$$

where  $\delta$  is the dirac delta function which is the first derivative of the Heavyside function  $H$  in one-dimensional form thus, only the zero level-set part could be considered. From the initial contour  $\Phi(x, y, t = 0)$ , a new contour was able to be defined by using the above relation till it reached to stationary state via iteration of the artificial time  $t$ .

Based on the theory, the method was applied on the original data which had not been dealt with the noise reduction technique. Additionally, the same masking criteria which were applied before the local threshold method 2.3.1 were employed before using the method. This is because the method is not able to cope with the image data which contain a large contrast between the inner and outer part of the sample, as mentioned before. Thus, by covering the exterior part

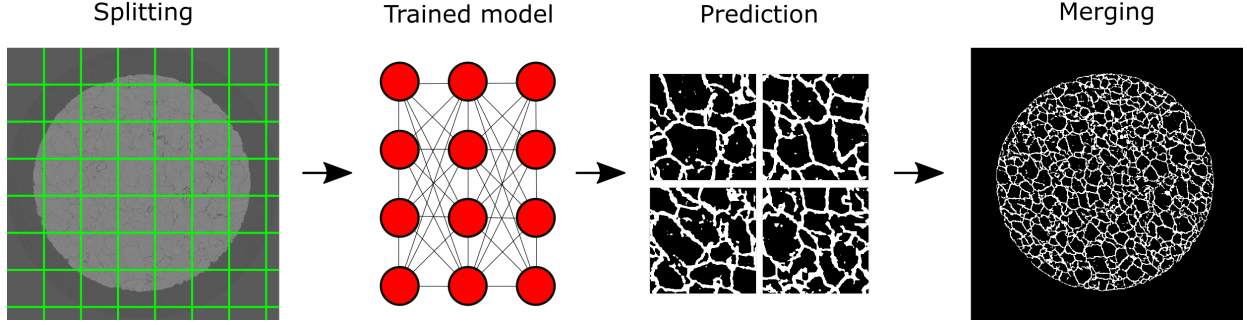


Figure 4: Workflow of machine learning based model. The green marked grid at splitting indicates edges of the fragment (400 x 400 voxels) from original image (2940 x 2940 voxels). After putting in each fragment into the trained model, we obtained prediction for each of fragments. By applying obtained threshold ( $\approx 0.5$  in the most cases) by Otsu method at each of predictions, these were able to be binarized. The binarized tiles were merged into original size of image.

with a manually extracted mean intensity of the non-fracture matrix, an effective segmentation of the fracture was able to be performed. Furthermore, in order to capture faint fractures which had a lower contrast than the other fractures, the method was applied on the cropped images with a size of (400  $\times$  400 voxels). These segmented small tiles were merged later into the original size of the image.(See the figure 5)

## 2.4 The Random Forest model

The Random Forest method [54], which is capable of multi-classification, was adopted for the segmentation of our scanned data. The model is using statistical results of multiple classifiers, commonly referred to as a decision tree.

The decision tree, which is a single classifier, is made of decision nodes and branches which are bifurcated from the nodes. In image segmentation, each node represents an applied filter, such as Gaussian, Hessian, etc., in order to create branches which represent the responses of the filter. This applied filters are also called feature maps (or layers) since these are used to extract unique responses from given image data [65]. Consequently, from the obtained responses from each filters (feature maps), one could categorize the information while matching the outputs with the provided truths (training data).

Based on this fundamental concept, the random forest method uses multiple decision trees instead of using a single decision tree. This is because of the over-fitting problem which makes the trained model work only for a specific case. For instance, a decision tree may perform well for a specific data set. However, it would not effectively classify data with outliers, such as noise or artifacts [81]. In the case of the random forest method, this risk could be reduced since the classification would be performed by aggregating the outputs of multiple decision trees. Therefore, even if we have a noise-sensitive decision tree in our created forest, this could be smoothed out since the corresponding data gets evaluated by many other trees.

In our study, the chosen feature maps, in order to create decision trees, were edge detectors (Gaussian difference and Hessian filtering), noise reduction filters (Gaussian blurring) and membrane detectors (membrane projections). The model is trained with the Trainable Weka platform (See [65] for the details of the adopted feature maps). The first slice of scanned data at the top side of the sample was used for training with the corresponding result obtained from the active contouring method (See 2.3.3). The data which was treated with the same procedure at 2.5 was applied to the trained model, and the predictions were later merged (see. 2.5). This step was necessary since the model was not able to cope with a slice of data which has a size of (2940 ) due to memory limitation.

## 2.5 The U-net model

The U-net model, one of the Convolutional Neural Network (CNN) architectures, proposed by [58] was applied to segment the fractures. This model would find optimized predictions between input and target by supervising the model with a ground truth (GT). The GT was chosen from the segmentation results of the above mentioned active contouring combined method 2.3.3 while the input data was raw images which were not treated with any noise reduction techniques.

The model consists of repeating down-scaling of the input image with the help of max-pooling layers and up-scaling with a de-convolutional layer. Additionally, before and after each of the up-/down-scaling layers, the convolutional

layers which extract the feature maps were used with an activation function which introduced a non-linearity to the model. Each of the extracted and down-scaled features were concatenated to the same size of the up-scaled features, in order to help the output pixels to be located at reasonable locations.

In our case, we adopted a  $2 \times 2$  kernel (with 2 stride) for max-pooling and the de-convolutional layers. The depth of the convolutional layer was set to 32 which implies the number of the extracted features. The kernel size of the convolutional layers were decided to be  $3 \times 3$ . As the size of extracted features down-scaled by following max-pooling layer, the depth of the convolutional layer was doubled (the maximum depth was 512). In contrast, the depth adjusted to be reduced after up-scaling. In addition, the adopted activation function for the convolutional layer was the Rectifier Linear Unit (relu) which has a range of output from 0 to 1 while it returns 0 for negative inputs and linear increment up to 1 for positives. At the final output layer, the sigmoid activation function was chosen, which has a non-linear shape and its output range is from 0 to 1. Consequently, the obtained output was a probability map where a number close to 1 was considered as the fracture and the rest were accounted for as non-fracture.

The images which were used for training were cropped into small tiles due to memory limitations (See 2.5). This made each tile to contain varying characteristics which also introduced a difficulty to train a model while taking these different characteristics into account.

In order to cope with this problem, the normalization layer, which zero-centers the histogram of the data in the range of -1 to 1, was used previous to insert the data into the model. This was especially essential to deal with the tiles with ring shape artifacts, which were induced during the reconstruction of the XRCT data. Without this layer, the model may not be able to identify the fractures in such regions due to the different profile they bear in comparison to the other regions, since the artifacts affect the histogram and shape of the features.

The implementation of the model is done by means of the *keras* library in Python [82] which includes useful functions for CNN such as convolutional, normalization layers, etc. With the given model details, the input data was separated into small pieces (*Splitting*), trained with GT data (*Training*) and finally it was merged back to the size of the original image (*Merging*).

**Splitting** Due to the in-house computer’s memory limitations, the big size of the complete data-set could not be dealt with the adopted machine learning model. This was because of the data which would be used for training and the model itself had to be allocated in the random-access memory RAM thus, a training data set which exceeded its memory limitation could not be applied. With the given information, the size of the applicable data for training was decided by means of non-/trainable parameters, induced by the number and size of the layers within the model. The size of the images and the batch size of the training data indicated the number of training data per one iteration of training (See 2.5). In our application moreover, since we wanted to take a benefit from the GPU, which could boost the training and processing time, the limitation of usable memory was even more restricted within the memory size of a GPU, which is normally smaller than the RAM and is not easily able to be expanded.

Consequently, due to these facts, the original size of 2D image data was split into small tiles. The original image size of  $2940 \times 2940$  pixels was cropped into multiple  $400 \times 400$  smaller images. We already knew that this could potentially induce some disconnection of the segmented fractures along the tiles, since the segmentation accuracy of the U-net model is low at the edges of given data due to the inevitable information loss during up-/down-scaling. In order to overcome and compensate this drawback, the overlapping scheme was applied, splitting the tiles to have 72 pixels of overlapping region at their borders. In this manner, 81 tiles were produced per 1 slice of a 2D original image. In addition, the format of the images which was “unsigned int 16” originally, was normalized into “unsigned int 8” after cutting the evaluated mean minimum and maximum intensities. This helped to reduce the memory demand caused by training data while preventing an over-simplification of the inherent histogram profiles.

**Training** Training was performed with the training data set mapping the cropped original image and GT. Only few data (60 slices) of scanned data (where the data was located at the top part of the sample) was used as the training data set. This number of slices corresponded to 4860 cropped tiles. Among the data set, 80 percent of the data (3888 tiles) were applied for updating the internal coefficients of the model, and the rest of the data (972 tiles) were used to evaluate the performance of the trained model by comparison between the predictions and GT.

For the sake of accuracy, the data augmentation technique was applied on the training data set. This allowed us to enrich the training data set by employing a modification to the data thus, the model could be trained with sufficient data of different variations. Consequently, the model would be trained with more trainable data. This contributed in the prevention of over-fitting, which made the model to be capable of dealing only with a specific case. In our application, we varied the brightness of the training data. Thus, the model was able to be trained by data with variation. This was necessary to get good predictions from all cropped tiles.

The batch size in machine learning defines how many of training data to be used for updating the inner parameters of the model during training. This implies that the batch size would directly affect the memory usage since the defined numbers of training data would be held on the memory. Therefore, in this case, this number was selected carefully as 5 so as not to reach our GPU memory limitation. The steps per epoch was set at 777, estimated based on the following relation :  $\approx \frac{\text{training data:3888}}{\text{batch size:5}}$  in a way that all the provided trainable data could be applied on each epoch. Finally, the model was trained with 100 epochs so that the segmentation accuracy could be enhanced along the iterations.

We adopted “binary cross entropy” loss function in order to deal with the binarization of image (classification of non-/fractures). The loss function  $L$  is defined such as,

$$L = -g_t \log(p) - (1 - g_t) \log(1 - p), \quad (22)$$

where  $g_t$  is the given truth, and  $p$  is the predicted probability of the model. Thus, the model was updated in a way that the difference between truths and predictions could be narrowed down. The “Adam” optimizer ([83]) was used for this optimization. The adopted fixed learning rate was 1e-4.

**Merging** After training the model by following the procedure mentioned earlier 2.5, the model was able to predict the non-/fractures within the given tiles. In order to obtain the same size of output with the original image, we performed this merging procedure which was basically placing every prediction tile at their corresponding locations, after collecting the predictions from the entire data set from the model. Since we applied the overlapping scheme 2.5 in order to prevent disconnections between tiles, 36 pixels at the edges were dropped for each tile which were considered as inaccurate predictions before merging. After the merging, the predictions which were in the range of 0 to 1 due to the output layer of the training model were binarized with the Otsu method ([29]) for the final segmentation output. The pixels which were classified as zeros in the predictions were excluded from this binarization by assuming that these pixels were certainly non-fracture.

### 3 Results and discussion

For our Carrara marble sample, which contained fracture networks, we successfully conducted image segmentation with all of the above mentioned segmentation means. By performing 2D segmentation on each slice of scanned data and stacking the segmentation results, the full 3D segmented fracture network was able to be acquired for the entire domain of the scanned data.

The parameters of the methods based on conventional schemes, such as Local threshold, Sato and active contouring, were fine tuned empirically. It was very time consuming to decide these parameters, since one had to find the appropriate parameters which would give the best results along the entire stack of the data while some slices contained different histogram profiles, or artifacts, which could had been caused by the density of fractures or the void differences in each slice, and minor defects on the detector.

Since the conventional schemes showed a tendency to be very sensitive to artifacts, which were induced by the inherent noise of the scanned data, and the corresponding outputs varied significantly with the applied parameters, applying the noise reduction technique ( 2.2) with carefully chosen parameters, was a fundamental step before applying any conventional method in order to minimize the error and obtain good results with.

In the case of machine learning-based segmentation, the applied methods had the ability to classify the fracture networks within the original data. From the experience we have, since these machine learning-based algorithms do not require any noise reduction technique, this was one of the biggest advantages of the schemes which could help not only to reduce the computation time but also the time for tuning the input parameters of the filtering method.

In figure 5, the segmentation results of the top-viewed specimen (x-y-planar size of  $2940 \times 2940$ ) are shown. We were able to acquire sufficiently good segmented results for the whole x-y-plane despite the beam hardening effect at the edges, and the ring artifacts in the middle of the sample, which were induced during reconstruction of the data. We selected the 1000th slice of the scanned data on the z-axis which is located at the middle of the sample. Note that this slice was never used as training data for the machine learning-based methods.

In figure 6, the segmentation results from the side-viewed sample (x-z-planar size of  $2940 \times 2139$ ) are demonstrated. These images were obtained by stacking the 2D segmentation results of x-y-planar images along the z-axis and extracting the 1400th slice on the y-axis. By showing the results from side and top, we demonstrate that there was no major discontinuity of the segmented fractures which could be caused by performing 2D segmentation and splitting.

Based on the 2D results in both figures 5 and 6, we were able to identify some advantages and disadvantages of each segmentation method. With the local threshold method we were able to obtain the segmented results which included most of the features within the data. The method definitely has the benefit of easy implementation and fast computation

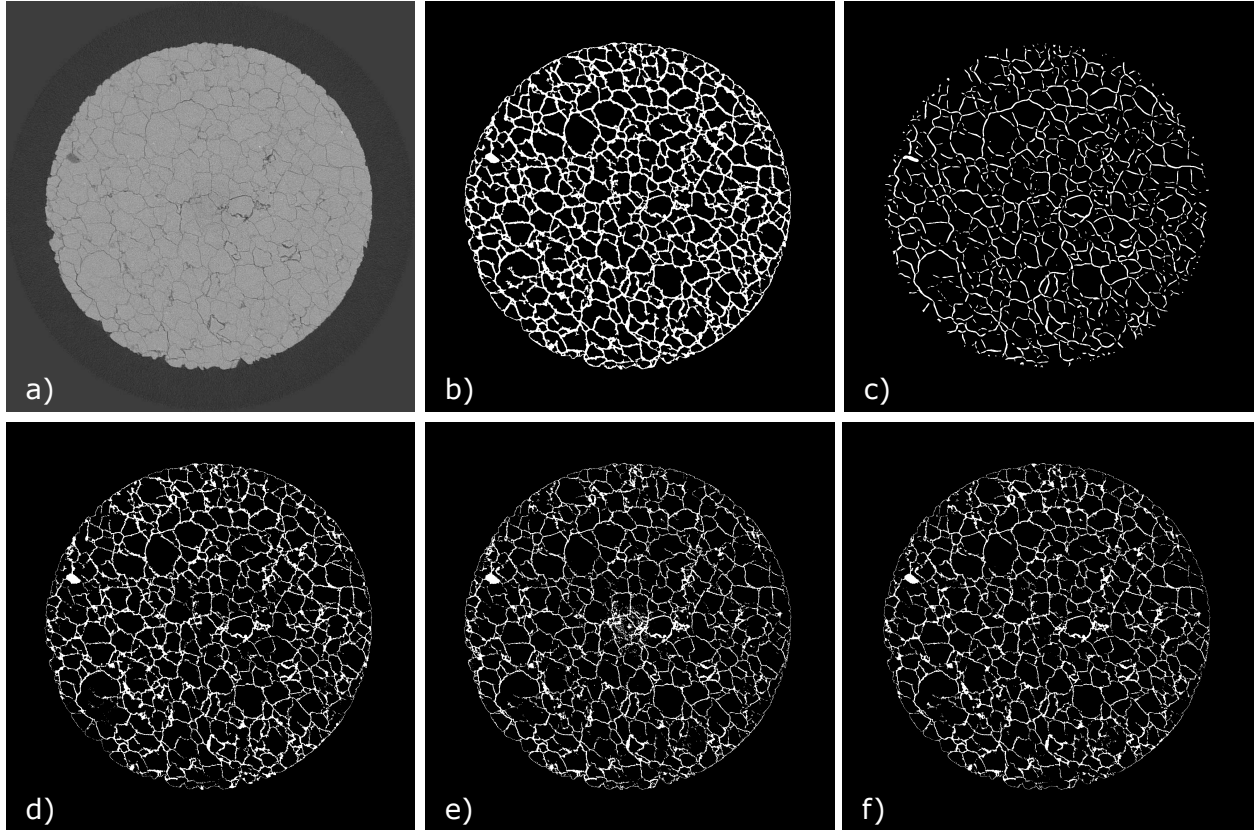


Figure 5: xy-plane data extracted at 1000th slice along z axis (total 2139), a) original data , b) LT, c) Sato, d) Active contouring, e) Random forest and f) U-net result.

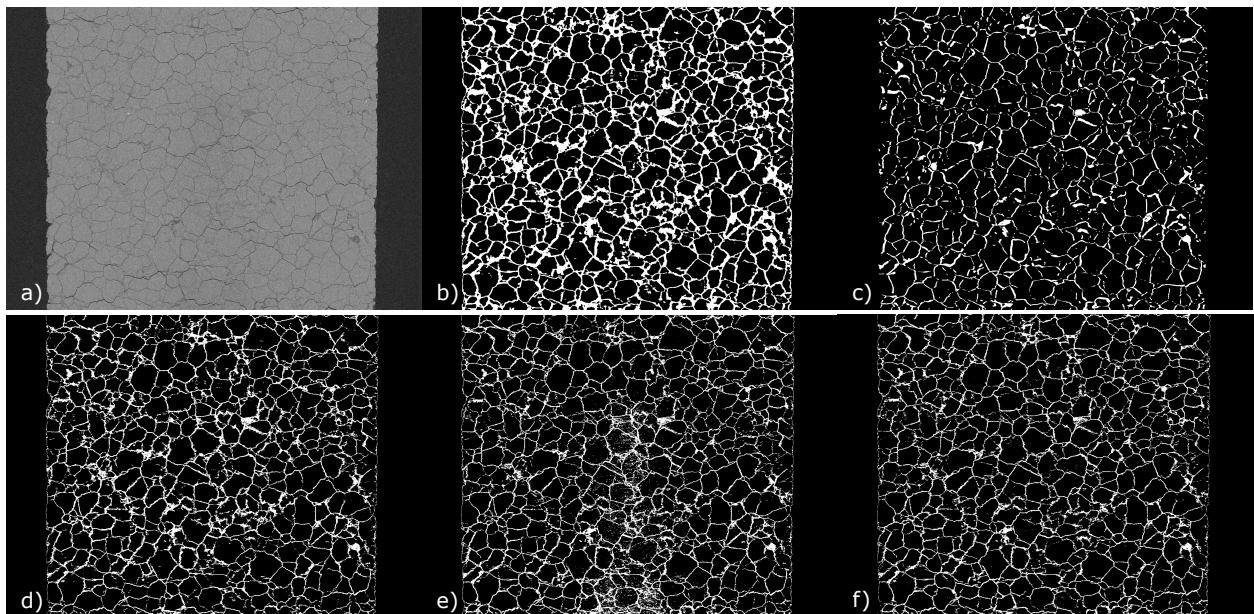


Figure 6: xz-plane data extracted at 1400th slice along y axis (total 2940), a) original data , b) LT, c) Sato, d) Active contouring, e) Random forest and f) U-net result.

time. In addition, the method was very consistent providing a continuous shape for the fracture network. However, the thickness of the segmented fracture was unrealistic. Also, due to the small contrast of the features, the method faced challenges distinguishing the features precisely when the fractures were located close to each other.

In the case of the Sato method, which is based on the Hessian matrix approach, despite the promising results from Voorn et al. [43], there was no significant benefit of this method in our application. The method was able to capture some of the fractures which had an elevated contrast however, it was not able to identify the faint fractures which had a lower contrast. In addition, the method also showed a limitation to classify the fractures at the points where multiple fractures were bifurcating. This was expected due as a characteristic feature of a Hessian matrix-based method as we mentioned in the beginning of the article (See 1). Additionally, the pores detected by this method tended to appear narrower than their real size. Please note that the outer edges between the exterior and inner part of the specimen were excluded with this method.

With the help of the active contouring method, we were able to obtain better results than the other conventional segmentation methods. The fractures were detected with thinner profiles, and pores were also able to be identified accordingly despite of the ring artifacts at the central area of the image (as shown in Figure 5). However, the fractures close to the outer rim still appeared being thicker than at other locations. This is caused by the beam hardening effect which induces spatial-varying brightness. Specifically, since the contour is defined depending on the mean intensity of the inner and outer areas in the initial binarized image, this spatial-varying intensity induced a bulged aperture where the mean intensity was higher (at the location close to the outer rim).

In addition, some parts which contained faint fractures were recognized with a weak connection which meant that the segmented fractures were not well identified. This was induced due to a variation of contrast of the fractures within the region of interest. Thus, a contour held with larger contrast remained and the others would vanish. Although we cropped the images into small tiles before applying the method in order to minimize the loss of low contrast fractures while evaluating the mean intensities for contours, this step did not guarantee that a clear separation between two different profiles in a tile would take place, thus, the fractures with low contrast tended to be ignored when the fractures of larger contrast were mostly taken into account for forming a contour. Despite the above observed drawbacks, the output of the method gave us sufficiently well segmented features of the fractures thus, we adopted this result as a truth image for the machine learning based models. Since the defects on the segmented results were minor and the machine learning models were able to learn a major characteristic from training data, the effect from the minority was expected to be statistically small.

In the case of the random forest method, where training happens with the use of a single slice of output of the active contouring method, the trained model was able to detect the fractures with finer profiles better than any other conventional method. More specifically, it was able to detect well the fractures when two fractures were located close to each other, which were identified as a merged one with the previously mentioned conventional methods. However, as shown in figures 5 and 6, it seemed that the method is sensitive to ring artifacts of the scanned data from the fact that we could observe significant amounts of fuzzy voxels which were classified as fractures at the central part of the image.

The segmentation results of the U-net method outperformed any other adopted methods in this comparison. With the help of the trained model, we were able to obtain clear segmentation results despite beam hardening and ring artifacts. In Figure 5, all the fractures which were of high and low contrast were efficiently classified while maintaining their scales of apertures. In addition, with the help of the overlapping scheme, we obtained continuous fractures even though we trained the model and computed the predictions with cropped images.

For the sake of detailed visualization, we demonstrated the segmentation results in a 3D sub-volume ( $600\hat{3}$  voxels) in Figure 7 with overlaid results on contrast enhanced original image in x-y- and x-z-planes at the middle (300th) of the sub-volume. The contrast of images was improved by using the histogram equalization method which adjusted the intensities of the image by redistributing those within a certain range [84].

In the 3D visualized structure with each of the adopted methods in Figure 7, we were able to obtain an overview of their unique responses. The segmented fractures from each method are marked in red. In the case of the local threshold method, as mentioned earlier, the method was able to recognize all the features however, the fractures were identified with a broader size compared to those in the original data. In addition, the outlines of the results were captured with rough surface profiles. Although the segmentation result with the method showed sufficiently well-matched shapes in general, from the middle of the x-z-plane overlaid image, we could conclude that the method was not so appropriate to detect sophisticated profiles, especially when the fractures were next to each other since these features were identified as a cavity.

In the case of the Sato method, as we showed in Figure 5 and 6, we were able to conclude from the 3D visualized data as well that the method was not so efficient to detect the fractures. The roughness of the surface was not able to be

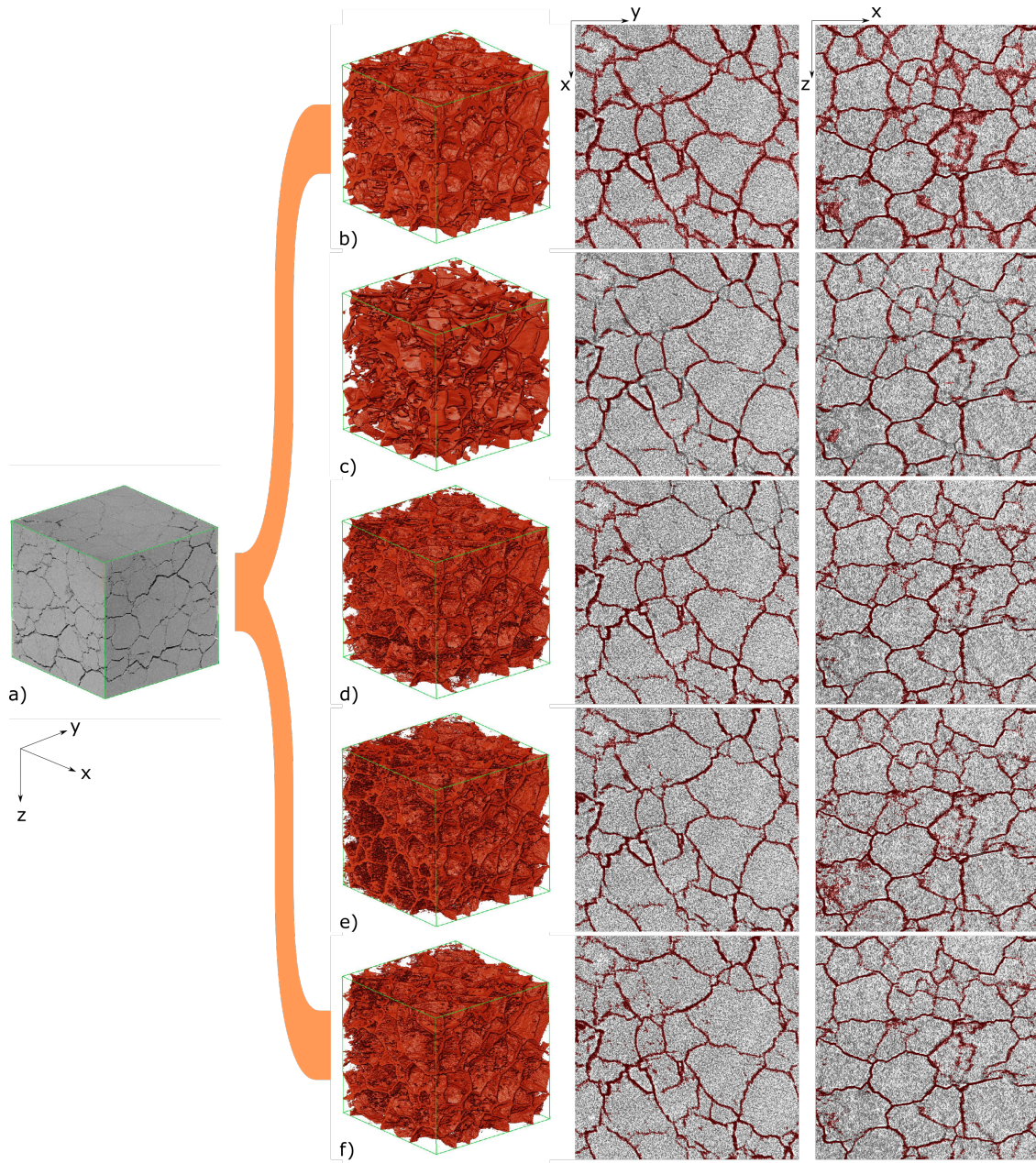


Figure 7: An extracted sub-volume from (1400, 1400, 1000) with size of  $600^3$  voxels where a) original data. The rests are from the segmentation results of b) Local threshold, c) sato, d) Active contouring, e) Random forest and f) U-net. The middle column displays 300th slice in xy-plane. The right column shows 300th slice in xz-plane. Each result is overlaid on corresponding histogram enhanced original image for a clear comparison.

accounted for and an unrealistic disconnection between the fractures was observed due to unidentified fractures with this method.

In the 3D visualized result with the active contouring method in Figure 7, the fractures were generally well classified and visualized. However, as it is shown in the overlaid images at the right top corner, some fractures were not detected due to their low contrast. In addition, the outlines of the fractures with sophisticated shapes were not able to be classified well.

Although we show in figures 5 and 6 that the result with the random forest method has challenges dealing with ring artifacts, the result in general showed accurate fracture profiles as it is demonstrated in figure 7 with an overlaid x-y-plane image. The segmentation results showed that the method was able to detect fractures with both high and low contrast. However, in the overlaid x-z-plane image, we could observe that the left bottom side contained lots of defects which was also found at the 3D visualization from the rough surface at the left corner. Thus, we were able to find that the segmentation was not well performed at some locations.

In the case of the U-net model, the segmented fractures were well matched with the fractures in the original data. Consequently, a clear outlook of fractures was also obtained in the 3D visualized data.

The noise reduction and segmentation workflows were performed with the hardware specification of intel(R) Core(TM) i7-8750H CPU @2.2GHz, 64GB of RAM and Nvidia Quadro P1000 (4GB). Based on this environment, the noise reduction, which was a fundamental step of the conventional segmentation methods and acquiring truth data, took 8 hours for the entire data set. The total computation time to obtain the segmentation results with each method were such as; 1.3 hours with local threshold, 35.6 hours with Sato, 118.2 hours with active contour, 433.7 hours with random forest and 4.1 hours with the U-net method. Note that the merging and cropping steps which were necessary in order to employ the active contour, random forest and U-net method are included in this time estimate (approximately 40 min). The training times for the machine learning based methods took 3.5 hours for the random forest and 21 hours for the U-net method.

We also computed the porosity based on the segmented results. By counting the number of fracture-classified voxels and dividing with the total number of voxels, we were able to compute an approximated porosity out of the images. The outer rim was excluded in the counting by applying a mask which was obtained by the combination of the Otsu method for binarization, and the fill and erosion method [85]. With the help of this evaluation, we acquired the porosity of the local threshold method : 25 %, Sato method : 12 %, active contouring method : 15 %, random forest method : 16 % and U-net method : 14 %. These values were larger than the porosity from actual measurement which was 4 %. The actual measurement was performed by measuring the volume changes before/after quenching.

This gap between the estimated value and the measurement was expected since we realized that the resolution of the scan data was not high enough to estimate the size of an aperture accurately. In addition, our intention was to obtain geometrical information of fracture networks within an wide field of view. Nevertheless, we used these results to speculate the accuracy of the segmentation.

As we showed in figure 7, the apertures in the result of the local threshold method were significantly overestimated. In the case of the random forest and active contour methods, although the methods were able to recognize fractures with thin profiles, the porosity was exaggerated due to poorly classified pixels due to the ring artifacts and fuzzy surfaces. The porosity from the Sato method showed the lowest value however, we demonstrated that there were many undetected features with the method. By considering these facts, the result from the U-net method again gave us the best result among the compared methods.

## 4 Conclusion

In this work we demonstrate segmentation workflows with three different conventional segmentation methods and two different machine learning based methods for XRCT data of dried fracture network which was induced by thermal quenching in Carrara marble. Despite the low contrast of the fractures in the available data, due to the fact that their apertures being very close to the limitation of the XRCT resolution, we were able to acquire successfully segmented 3D fracture networks with proposed segmentation workflows.

With the acquired segmentation results acquired by the proposed segmentation workflows, we conducted a quality and efficiency comparison and showed that the results with the U-net method were the most efficient and accurate. Among the applied conventional segmentation schemes, we were able to obtain the best quality of results with the active contouring method and the best time efficiency with the local threshold method. For the adopted machine learning based schemes, we trained the models with results from the active contouring method. This was advantageous compared to manual labelling, especially since manual labelling was far from being the best option given that the

fractures were of low contrast. Therefore, it was hard to identify a clear outline of faint features in an extensive domain. Consequently, manual labelling work would be too arduous to obtain sufficient and accurate training data. In addition, we also showed that the defects which were detected with the conventional methods were improved with the trained machine learning-based methods.

In order to perform the segmentation with conventional methods, the application of the adaptive manifold non-local mean filter, which is one of the noise reduction techniques, was a fundamental step due to the inherent noise of the scanned data. However, with the machine learning methods, this step was not necessary. We were able to obtain fully segmented data by providing less filtered data to the training model. This was quite advantageous compared to the conventional approaches since the computation time and resources were significantly reduced. Additionally, the fine-tuning of the input parameters, which were mandatory for the conventional methods, did not play a significant role in the attempt to get good segmentation results.

With our application, we showed that obtaining a full 3D structure of segmented data was able to be performed efficiently by employing the proposed segmentation workflows in 2D images. Thus, the big volume of data could be dealt with, with a conventional home PC without requiring any the advanced properties of a special computer. Although we also showed that the resolution of the data to estimate the exact size of apertures of fracture networks was not sufficient by comparing with the actual measurement of porosity, the rough geometrical information was acquired without demanding any additional procedure. For future work, we intend to correlate the acquired geometrical information regarding fractures with porosimetry results. In addition, characterization of fractures in terms of lengths and angle could be further investigated.

## References

- [1] B. Berkowitz, “Analysis of Fracture Network Connectivity Using Percolation Theory,” *Mathematical Geology*, vol. 27, no. 4, pp. 467–483, 1995.
- [2] Y. Jing, R. T. Armstrong, and P. Mostaghimi, “Rough-walled discrete fracture network modelling for coal characterisation,” *Fuel*, vol. 191, pp. 442–453, 2017.
- [3] S. Karimpouli, P. Tahmasebi, H. L. Ramandi, P. Mostaghimi, and M. Saadatfar, “Stochastic modeling of coal fracture network by direct use of micro-computed tomography images,” *International Journal of Coal Geology*, vol. 179, no. April, pp. 153–163, 2017.
- [4] T. Jiang, J. Zhang, and H. Wu, “Experimental and numerical study on hydraulic fracture propagation in coalbed methane reservoir,” *Journal of Natural Gas Science and Engineering*, vol. 35, pp. 455–467, 2016.
- [5] Y. Dong, P. Li, W. Tian, Y. Xian, and D. Lu, “Journal of Natural Gas Science and Engineering An equivalent method to assess the production performance of horizontal wells with complicated hydraulic fracture network in shale oil reservoirs,” *Journal of Natural Gas Science and Engineering*, vol. 71, no. May, p. 102975, 2019.
- [6] Q. Lei and K. Gao, “Correlation between fracture network properties and stress variability in geological media,” *Geophysical Research Letters*, vol. 45, no. 9, pp. 3994–4006, 2018.
- [7] B. R. Crawford, M. C. Tsenn, J. M. Homburg, R. C. Stehle, J. A. Freysteinson, and W. C. Reese, “Incorporating Scale-Dependent Fracture Stiffness for Improved Reservoir Performance Prediction,” *Rock Mechanics and Rock Engineering*, vol. 50, no. 12, pp. 3349–3359, 2017.
- [8] N. Huang, R. Liu, Y. Jiang, Y. Cheng, and B. Li, “Shear-flow coupling characteristics of a three-dimensional discrete fracture network-fault model considering stress-induced aperture variations,” *Journal of Hydrology*, vol. 571, no. February, pp. 416–424, 2019.
- [9] W. M. S. B. Weerakone and R. C. K. Wong, *Characterization of Variable Aperture Rock Fractures Using X-ray Computer Tomography*, pp. 229–235. John Wiley & Sons, Ltd, 2006.
- [10] H. F. Taylor, C. O’Sullivan, and W. W. Sim, “A new method to identify void constrictions in micro-CT images of sand,” *Computers and Geotechnics*, vol. 69, pp. 279–290, 2015.
- [11] T. De Kock, M. A. Boone, T. De Schryver, J. Van Stappen, H. Derluyn, B. Masschaele, G. De Schutter, and V. Cnudde, “A pore-scale study of fracture dynamics in rock using X-ray micro-CT under ambient freeze-thaw cycling,” *Environmental Science and Technology*, vol. 49, no. 5, pp. 2867–2874, 2015.
- [12] E. H. Saenger, S. Vialle, M. Lebedev, D. Uribe, M. Osorno, M. Duda, and H. Steeb, “Digital carbonate rock physics,” *Solid Earth*, vol. 7, no. 4, pp. 1185–1197, 2016.
- [13] S. Y. Chung, J. S. Kim, D. Stephan, and T. S. Han, “Overview of the use of micro-computed tomography (micro-CT) to investigate the relation between the material characteristics and properties of cement-based materials,” *Construction and Building Materials*, vol. 229, p. 116843, 2019.

- [14] J. Lai, G. Wang, Z. Fan, J. Chen, Z. Qin, C. Xiao, S. Wang, and X. Fan, “Three-dimensional quantitative fracture analysis of tight gas sandstones using industrial computed tomography,” *Scientific Reports*, vol. 7, no. 1, pp. 1–12, 2017.
- [15] W. G. Kumari, P. G. Ranjith, M. S. Perera, and B. K. Chen, “Experimental investigation of quenching effect on mechanical, microstructural and flow characteristics of reservoir rocks: Thermal stimulation method for geothermal energy extraction,” *Journal of Petroleum Science and Engineering*, vol. 162, no. December 2017, pp. 419–433, 2018.
- [16] G. Zhang, P. G. Ranjith, M. S. Perera, A. Haque, X. Choi, and K. S. Sampath, “Characterization of coal porosity and permeability evolution by demineralisation using image processing techniques: A micro-computed tomography study,” *Journal of Natural Gas Science and Engineering*, vol. 56, no. June, pp. 384–396, 2018.
- [17] O. Furat, M. Wang, M. Neumann, L. Petrich, M. Weber, C. E. Krill, and V. Schmidt, “Machine learning techniques for the segmentation of tomographic image data of functional materials,” *Frontiers in Materials*, vol. 6, no. June, 2019.
- [18] A. S. Frangakis and R. Hegerl, “Noise reduction in electron tomographic reconstructions using nonlinear anisotropic diffusion,” *Journal of Structural Biology*, vol. 135, no. 3, pp. 239–250, 2001.
- [19] C. P. Behrenbruch, S. Petroudi, S. Bond, J. D. Declerck, F. J. Leong, and J. M. Brady, “Image filtering techniques for medical image post-processing: An overview,” *British Journal of Radiology*, vol. 77, no. SPEC. ISS. 2, 2004.
- [20] P. Christe, M. Bernasconi, P. Vontobel, P. Turberg, and A. Parriaux, “Three-dimensional petrographical investigations on borehole rock samples: A comparison between X-ray computed- and neutron tomography,” *Acta Geotechnica*, vol. 2, no. 4, pp. 269–279, 2007.
- [21] J. Coady, A. O’Riordan, G. Dooly, T. Newe, and D. Toal, “An overview of popular digital image processing filtering operations,” *Proceedings of the International Conference on Sensing Technology, ICST*, vol. 2019-Decem, 2019.
- [22] M. Poulouse, “Literature Survey on Image Deblurring Techniques,” *International Journal of Computer Applications Technology and Research*, vol. 2, no. 3, pp. 286–288, 2013.
- [23] B. B. Ahamed, D. Yuvaraj, and S. S. Priya, “Image Denoising with Linear and Non-linear Filters,” *Proceedings of 2019 International Conference on Computational Intelligence and Knowledge Economy, ICCIKE 2019*, vol. 10, no. 6, pp. 806–810, 2019.
- [24] P. Perona and J. Malik, “Scale-Space and Edge Detection Using Anisotropic Diffusion,” *IEEE Transactions on Pattern Analysis and Machine Intelligence*, vol. 12, no. 7, pp. 629–639, 1990.
- [25] A. Buades, B. Coll, and J.-M. Morel, “Non-Local Means Denoising,” *Image Processing On Line*, vol. 1, pp. 208–212, 2011.
- [26] E. S. Gastal and M. M. Oliveira, “Adaptive manifolds for real-time high-dimensional filtering,” *ACM Transactions on Graphics*, vol. 31, no. 4, 2012.
- [27] A. P. Sheppard, R. M. Sok, and H. Averdunk, “Techniques for image enhancement and segmentation of tomographic images of porous materials,” *Physica A: Statistical Mechanics and its Applications*, vol. 339, no. 1-2, pp. 145–151, 2004.
- [28] H. L. Ramandi, P. Mostaghimi, and R. T. Armstrong, “Digital rock analysis for accurate prediction of fractured media permeability,” *Journal of Hydrology*, vol. 554, pp. 817–826, 2017.
- [29] Nobuyuki Otsu, “A Threshold Selection Method from Gray-Level Histograms,” *IEEE Trans. Syst. Man Cybern*, vol. 9, no. 1, pp. 62–66, 1979.
- [30] N. Salman, “Image Segmentation Based on Watershed and Edge Detection Techniques,” *The International Arab Journal of Information Technology*, vol. 3, no. 2, pp. 104–110, 2006.
- [31] N. Dhanachandra, K. Mangleam, and Y. J. Chanu, “Image Segmentation Using K-means Clustering Algorithm and Subtractive Clustering Algorithm,” *Procedia Computer Science*, vol. 54, pp. 764–771, 2015.
- [32] S. Chauhan, W. Rūhaak, F. Khan, F. Enzmann, P. Mielke, M. Kersten, and I. Sass, “Processing of rock core microtomography images: Using seven different machine learning algorithms,” *Computers and Geosciences*, vol. 86, pp. 120–128, 2016.
- [33] J. MacQueen, “Some methods for classification and analysis of multivariate observations,” in *Proceedings of the Fifth Berkeley Symposium on Mathematical Statistics and Probability, Volume I: Statistics*, (Berkeley, Calif.), pp. 281–297, University of California Press, 1967.
- [34] R. A. Ketcham and R. D. Hanna, “Beam hardening correction for X-ray computed tomography of heterogeneous natural materials,” *Computers and Geosciences*, vol. 67, pp. 49–61, 2014.

- [35] T. C. Su, M. D. Yang, T. C. Wu, and J. Y. Lin, "Morphological segmentation based on edge detection for sewer pipe defects on CCTV images," *Expert Systems with Applications*, vol. 38, no. 10, pp. 13094–13114, 2011.
- [36] S. S. Al-amri, N. V. Kalyankar, and K. S.D, "Image segmentation by using edge detection," *International Journal on Computer Science and Engineering*, vol. 2, no. 3, pp. 804–807, 2010.
- [37] J. Canny, "A computational approach to edge detection," *IEEE Transactions on Pattern Analysis and Machine Intelligence*, vol. PAMI-8, no. 6, pp. 679–698, 1986.
- [38] R. Dura and P. Hart, *Pattern Classification and Scene Analysis*. John Wiley and Sons, first ed., 1973.
- [39] R. Kimmel and A. M. Bruckstein, "Regularized Laplacian zero crossings as optimal edge integrators," *International Journal of Computer Vision*, vol. 53, no. 3, pp. 225–243, 2003.
- [40] Y. Sato, S. Nakajima, H. Atsumi, T. Roller, G. Gerig, S. Yoshida, and R. Kikinis, "3D Multi-Scale Line Filter for Segmentation and Visualization of Curvilinear Structures in Medical Images," *Lecture Notes in Computer Science (including subseries Lecture Notes in Artificial Intelligence and Lecture Notes in Bioinformatics)*, vol. 1205, no. 2, pp. 213–222, 1997.
- [41] A. F. Frangi, W. J. Niessen, K. L. Vincken, and M. A. Viergever, "Multiscale vessel enhancement filtering," *Lecture Notes in Computer Science (including subseries Lecture Notes in Artificial Intelligence and Lecture Notes in Bioinformatics)*, vol. 1496, pp. 130–137, 1998.
- [42] M. Erdt, M. Raspe, and M. Suehling, "Automatic hepatic vessel segmentation using graphics hardware," in *Medical Imaging and Augmented Reality* (T. Dohi, I. Sakuma, and H. Liao, eds.), (Berlin, Heidelberg), pp. 403–412, Springer Berlin Heidelberg, 2008.
- [43] M. Voorn, U. Exner, and A. Rath, "Multiscale Hessian fracture filtering for the enhancement and segmentation of narrow fractures in 3D image data," *Computers and Geosciences*, vol. 57, pp. 44–53, 2013.
- [44] H. Deng, J. P. Fitts, and C. A. Peters, "Quantifying fracture geometry with X-ray tomography: Technique of Iterative Local Thresholding (TILT) for 3D image segmentation," *Computational Geosciences*, vol. 20, no. 1, pp. 231–244, 2016.
- [45] S. Z. Li and A. Jain, eds., *Local Adaptive Thresholding*, pp. 939–939. Boston, MA: Springer US, 2009.
- [46] K. Drechsler and C. Oyarzun Laura, "Comparison of vesselness functions for multiscale analysis of the liver vasculature," in *Proceedings of the 10th IEEE International Conference on Information Technology and Applications in Biomedicine*, pp. 1–5, 2010.
- [47] S. Beucher and F. Meyer, *The Morphological Approach to Segmentation: The Watershed Transformation*, vol. 18. Inc., New York, 1993.
- [48] C. R. Maurer, R. Qi, and V. Raghavan, "A linear time algorithm for computing exact Euclidean distance transforms of binary images in arbitrary dimensions," *IEEE Transactions on Pattern Analysis and Machine Intelligence*, vol. 25, no. 2, pp. 265–270, 2003.
- [49] V. Caselles, F. Catté, T. Coll, and F. Dibos, "A geometric model for active contours in image processing," *Numerische Mathematik*, vol. 66, no. 1, pp. 1–31, 1993.
- [50] S. Li, W. Song, L. Fang, Y. Chen, P. Ghamisi, and J. A. Benediktsson, "Deep learning for hyperspectral image classification: An overview," *IEEE Transactions on Geoscience and Remote Sensing*, vol. 57, no. 9, pp. 6690–6709, 2019.
- [51] S. P. Singh, L. Wang, S. Gupta, H. Goli, P. Padmanabhan, and B. Gulyás, "3d deep learning on medical images: A review," 2020.
- [52] S. Minaee, Y. Boykov, F. Porikli, A. Plaza, N. Kehtarnavaz, and D. Terzopoulos, "Image segmentation using deep learning: A survey," 2020.
- [53] O. Kodym and M. Spanel, "Semi-automatic ct image segmentation using random forests learned from partial annotations," in *BIOIMAGING*, 2018.
- [54] Y. Amit and D. Geman, "Shape Quantization and Recognition with Randomized Trees," *Neural Computation*, vol. 9, no. 7, pp. 1545–1588, 1997.
- [55] S. Albawi, T. A. Mohammed, and S. Al-Zawi, "Understanding of a convolutional neural network," in *Proceedings of 2017 International Conference on Engineering and Technology, ICET 2017*, vol. 2018-Janua, pp. 1–6, IEEE, 2018.
- [56] J. Long, E. Shelhamer, and T. Darrell, "Fully Convolutional Networks for Semantic Segmentation," *IEEE Transactions on Pattern Analysis and Machine Intelligence*, vol. 39, no. 4, pp. 640–651, 2017.

- [57] T. Werz, M. Baumann, U. Wolfram, and C. E. Krill, “Particle tracking during Ostwald ripening using time-resolved laboratory X-ray microtomography,” *Materials Characterization*, vol. 90, pp. 185–195, 2014.
- [58] O. Ronneberger, P. Fischer, and T. Brox, “U-net: Convolutional networks for biomedical image segmentation,” *Lecture Notes in Computer Science (including subseries Lecture Notes in Artificial Intelligence and Lecture Notes in Bioinformatics)*, vol. 9351, pp. 234–241, 2015.
- [59] J. Kang, N. Lu, I. Loo, N. Senabulya, and A. J. Shahani, “PolyProc: A Modular Processing Pipeline for X-ray Diffraction Tomography,” *Integrating Materials and Manufacturing Innovation*, vol. 8, no. 3, pp. 388–399, 2019.
- [60] V. Khryashchev, L. Ivanovsky, V. Pavlov, A. Ostrovskaya, and A. Rubtsov, “Comparison of Different Convolutional Neural Network Architectures for Satellite Image Segmentation,” in *Conference of Open Innovation Association, FRUCT*, vol. 2018-Novem, pp. 172–179, 2018.
- [61] C. Shorten and T. M. Khoshgoftaar, “A survey on Image Data Augmentation for Deep Learning,” *Journal of Big Data*, vol. 6, no. 1, 2019.
- [62] G. Roberts, S. Y. Haile, R. Sainju, D. J. Edwards, B. Hutchinson, and Y. Zhu, “Deep Learning for Semantic Segmentation of Defects in Advanced STEM Images of Steels,” *Scientific Reports*, vol. 9, no. 1, pp. 1–12, 2019.
- [63] Z. Zhou, M. M. R. Siddiquee, N. Tajbakhsh, and J. Liang, “UNet++: Redesigning Skip Connections to Exploit Multiscale Features in Image Segmentation,” *IEEE Transactions on Medical Imaging*, pp. 1–1, 2019.
- [64] N. Alqahtani, F. Alzubaidi, R. T. Armstrong, P. Swietojanski, and P. Mostaghimi, “Machine learning for predicting properties of porous media from 2d X-ray images,” *Journal of Petroleum Science and Engineering*, vol. 184, no. March 2019, p. 106514, 2020.
- [65] I. Arganda-Carreras, V. Kaynig, C. Rueden, K. W. Eliceiri, J. Schindelin, A. Cardona, and H. S. Seung, “Trainable Weka Segmentation: A machine learning tool for microscopy pixel classification,” *Bioinformatics*, vol. 33, no. 15, pp. 2424–2426, 2017.
- [66] M. Ruf and H. Steeb, “micro-XRCT data set of Carrara marble with artificially created crack network: fast cooling down from 600°C,” 2020.
- [67] M. Pieri, L. Burlini, K. Kunze, I. Stretton, and D. L. Olgaard, “Rheological and microstructural evolution of carrara marble with high shear strain: results from high temperature torsion experiments,” *Journal of Structural Geology*, vol. 23, no. 9, pp. 1393 – 1413, 2001.
- [68] C. Delle Piane, A. Arena, J. Sarout, L. Esteban, and E. Cazes, “Micro-crack enhanced permeability in tight rocks: An experimental and microstructural study,” *Tectonophysics*, vol. 665, pp. 149–156, dec 2015.
- [69] M. Ruf and H. Steeb, “Effects of thermal treatments on the wave propagation velocities for Carrara marble,” *Journal of Geophysical Research: Solid Earth*, 2021. to be submitted.
- [70] L. Pimienta, L. F. Orellana, and M. Violay, “Variations in elastic and electrical properties of crustal rocks with varying degree of microfracturation,” *Journal of Geophysical Research: Solid Earth*, vol. 124, pp. 6376–6396, jul 2019.
- [71] J. Sarout, E. Cazes, C. Delle Piane, A. Arena, and L. Esteban, “Stress-dependent permeability and wave dispersion in tight cracked rocks: Experimental validation of simple effective medium models,” *Journal of Geophysical Research: Solid Earth*, vol. 122, pp. 6180–6201, aug 2017.
- [72] S. Peacock, C. McCann, J. Sothcott, and T. Astin, “Seismic velocities in fractured rocks: an experimental verification of Hudson’s theory,” *Geophysical Prospecting*, vol. 42, pp. 27–80, jan 1994.
- [73] M. Ruf and H. Steeb, “An open, modular, and flexible micro x-ray computed tomography system for research,” *Review of Scientific Instruments*, vol. 91, p. 113102, nov 2020.
- [74] I. T. Jolliffe and J. Cadima, “Principal component analysis: A review and recent developments,” *Philosophical Transactions of the Royal Society A: Mathematical, Physical and Engineering Sciences*, vol. 374, no. 2065, 2016.
- [75] C. Davis, “The norm of the Schur product operation,” *Numerische Mathematik*, vol. 4, no. 1, pp. 343–344, 1962.
- [76] E. S. Gastal and M. M. Oliveira, “Domain transform for edge-aware image and video processing,” *ACM Transactions on Graphics*, vol. 30, no. 4, 2011.
- [77] G. H. Golub and C. F. Van Loan, *Matrix Computations*. The Johns Hopkins University Press, third ed., 1996.
- [78] T. F. Chan and L. A. Vese, “Active contours without edges,” *IEEE Transactions on Image Processing*, vol. 10, no. 2, pp. 266–277, 2001.
- [79] D. Mumford and J. Shah, “Optimal approximations by piecewise smooth functions and associated variational problems,” *Communications on Pure and Applied Mathematics*, vol. 42, no. 5, pp. 577–685, 1989.

- [80] S. Osher and R. Tsai, "Level Set Methods and Their Applications in Image Science," *Communications in Mathematical Sciences*, vol. 1, no. 4, pp. 1–20, 2003.
- [81] P. P. Shinde and S. Shah, "A Review of Machine Learning and Deep Learning Applications," *Proceedings - 2018 4th International Conference on Computing, Communication Control and Automation, ICCUBEA 2018*, 2018.
- [82] F. Chollet *et al.*, "Keras." <https://github.com/fchollet/keras>, 2015.
- [83] D. P. Kingma and J. Ba, "Adam: A method for stochastic optimization," 2017.
- [84] T. Acharya and A. K. Ray, *Image Processing - Principles and Applications*. USA: Wiley-Interscience, 2005.
- [85] L. Vincent and E. R. Dougherty, "Morphological Segmentation for Textures and Particles," *Digital Image Processing Methods*, pp. 43–102, 1994.